Supporting Information

Dimension Engineering of High-Quality InAs Nanostructures on a Wafer-Scale

Dong Pan,[†,#] Ji-Yin Wang,[‡] Wei Zhang,[§,¶] Lujun Zhu,[∥,▲] Xiaojun Su,[§] Furong Fan,[‡] Yuhao Fu,[⊥] Shaoyun Huang,[‡] Dahai Wei,[†] Lijun Zhang,[⊥] Manling Sui,[∥] Arkady Yartsev,[§] Hongqi Xu[‡,∇,◇] and Jianhua Zhao*[,†,#,◆,◇]

[†]*State Key Laboratory of Superlattices and Microstructures, Institute of Semiconductors, Chinese Academy of Sciences, P.O. Box 912, Beijing 100083, China*
[‡]*Beijing Key Laboratory of Quantum Devices, Key Laboratory for the Physics and Chemistry of Nanodevices and Department of Electronics, Peking University, Beijing 100871, China*
[§]*NanoLund and Division of Chemical Physics, Lund University, Box 124, 22100 Lund, Sweden*
[∥]*Institute of Microstructure and Properties of Advanced Materials, Beijing University of Technology, Beijing 100124, China*
[⊥]*Key Laboratory of Automobile Materials of MOE and School of Materials Science and Engineering, Jilin University, Changchun 130012, China*
[#]*Center of Materials Science and Optoelectronics Engineering, University of Chinese Academy of Sciences, Beijing, 100190, China*
[∇]*NanoLund and Division of Solid State Physics, Lund University, Box 118, S-22100 Lund, Sweden*
[◇]*Beijing Academy of Quantum Information Sciences, Beijing 100193, China*
[◆]*CAS Center for Excellence in Topological Quantum Computation, University of Chinese Academy of Sciences, Beijing 100190, China*
[¶]*School of Physics and Electronic Engineering, Guangzhou University, Guangzhou 510006, China*
[▲]*College of Physics and Information Technology, Shaanxi Normal University, Xi'an 710062, China*

[*]To whom correspondence should be addressed. E-mail: jhzhao@red.semi.ac.cn (J.H.Z.)

Contents

S1 Detailed substrate treating procedures and equipments for sample characterization

Substrate treating procedures

Si substrates: Commercial p-type Si (111) wafers were used as the substrates. Before loading the Si substrates into the MBE chamber, they were immersed in a diluted HF (2%) solution for 1 min to remove the surface contamination and native oxide.

MgO and sapphire substrates: Commercial MgO (100) and polished and unpolished sapphire (0001) wafers were used as the substrates. Before loading them into the MBE chamber, they were cleaned thoroughly by first rinsing them with deionized water and then sonicating in acetone, ethanol, and isopropanol, respectively. The sonication time of each step was 5 min and the substrates were dried with nitrogen at each step.

GaAs substrates: Commercial GaAs (100) wafers were used as the substrates. After loading the GaAs substrates into the MBE chamber, the substrate surface was first degassed in the preparation chamber for 2 hours at 200 °C. Then the substrate was transferred to the growth chamber to be thermally deoxidized at 580 °C, and a 200 nm thick GaAs buffer layer was grown on the substrate at 560 °C to achieve atomically flat surface. After that, a thin silver film was *in situ* deposited on the top of the GaAs buffer layer at 25 °C by opening the shutter of the silver effusion cell attached to the III-V growth chamber.

Equipments for sample characterization

The morphologies of the samples were observed by SEM with a Nova NanoSEM 650, operated at 20 kV. Structural characterization was performed using TEM and samples were removed from the growth substrate via sonication in ethanol and then drop-cast onto a holey carbon film supported by a copper grid. High-resolution TEM, HAADF-STEM images and EDS spectra (including the EDS elemental mapping and line scans shown in Fig. 2 in the main text and Supporting Information section S6) were taken with an FEI Titan G2 microscope equipped with a super-X detector, operated at 300 kV. Other high-resolution TEM images were collected using a JEOL2100, operated at 200 kV.

The time resolved THz measurements were conducted by a setup described in Refs 1 and 2. Laser pulses (796 nm, 80 fs pulse length, 1 kHz repetition rate) were generated by a regenerative amplifier (Spitfire Pro XP, Spectra Physics) seeded by a femtosecond oscillator (MaiTai, Spectra Physics). The laser beam was split into three. The first beam (400 µJ/pulse) was used to generate THz radiation by optical rectification in a MgO: $LiNbO_3$ crystal. The second beam was used for electro-optical sampling of the THz pulses in a (110) ZnTe crystal. The third beam, which was used for excitation was converted to the second harmonic (398 nm) in a BBO crystal. To avoid absorption of the THz radiation by water vapor, the setup was purged with dry nitrogen. To conduct TRTS measurement, nanowire and nanosheet samples were embedded in the colorless First Contact polymer (CFCP) film (Photonic Cleaning Technologies LLC) and peeled off from native substrates. CFCP film is an optically transparent, inert, plastic film, and no photoconductivity response of CFCP was observed in the reference TRTS measurement.

S2 Dimensional tunability of InAs from 1-D to 2-D

In Table S1, we have summarized the growth parameters for the InAs nanostructures grown with different indium fluxes in Fig. 1 in the main text and Fig. S1. Dimensions of InAs can be tuned from 1-D nanowires to 2-D nanosheets, to 1-D nanowire/2-D nanosheet crosses, and to double 2-D nanosheets/1-D nanowire crosses by increasing the indium flux and keeping other growth parameters constant.

Table S1. Summary of growth parameters for the InAs nanostructures grown with different indium fluxes.

Substrates	Series	Indium flux (mbar)	Arsenic flux (mbar)	V/III	Growth time (min)	Growth temperature (°C)
Si (111)	Variant indium flux	2.0×10^{-7}	5.9×10^{-6}	**29.5**	40	505
		4.9×10^{-7}	5.9×10^{-6}	**12.0**	40	505
		7.4×10^{-7}	5.9×10^{-6}	**8.0**	40	505
		9.3×10^{-7}	5.9×10^{-6}	**6.3**	40	505
		1.1×10^{-6}	5.9×10^{-6}	**5.4**	40	505
		1.3×10^{-6}	5.9×10^{-6}	**4.5**	40	505
		2.0×10^{-6}	5.9×10^{-6}	**3.0**	40	505

Figure S1 is 25° tilted SEM images of InAs nanostructures grown with the indium flux of 1.1×10^{-6} mbar, 1.3×10^{-6} mbar, and 2.0×10^{-6} mbar, respectively (keeping the arsenic flux constant, 5.9×10^{-6} mbar) on Si (111) substrates using silver as catalysts. We can see that sample grown with the indium flux of 1.1×10^{-6} mbar consists with the kinked 2-D InAs nanosheets. Most of them are 1-D nanowire/2-D nanosheet hybrid structures. Increasing the indium flux to 1.3×10^{-6} mbar, the density of InAs nanostructures decreases obviously because the silver nanoparticles are covered by the parasitic InAs islands. Very lager irregular indium nanoparticles form on the top of the InAs 1-D structures owing to the sample grown under a very high indium flux. Further increasing the indium flux to 2.0×10^{-6} mbar (arsenic/indium BEP ratio=3.0), this low V/III BEP ratio is very close to typical V/III BEP ratio for the growth of InAs planar epitaxial layers. Therefore, only discontinuous InAs layer can be observed on the substrate surface.
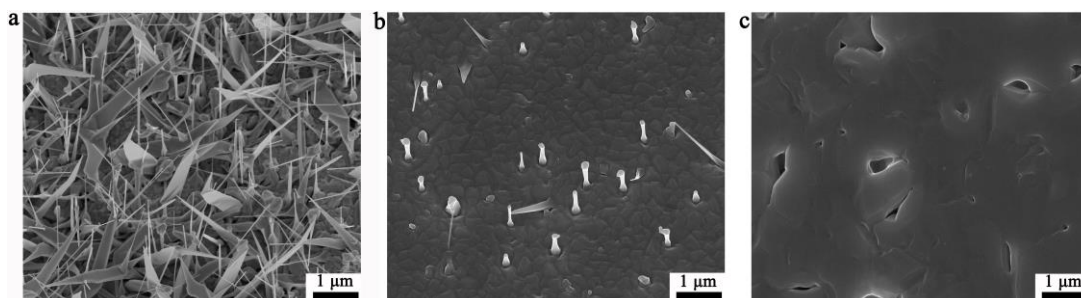
Figure S1. 25° tilted SEM images of InAs nanostructures grown at different indium fluxes (keeping the arsenic flux constant, 5.9×10^{-6} mbar) on Si (111) substrates using silver as catalysts. By increasing the indium flux (indium fluxes in **a-c** are 1.1×10^{-6} mbar, 1.3×10^{-6} mbar, and 2.0×10^{-6} mbar, respectively). For all the samples, the growth time is 40 min and the growth temperature is 505 °C.

S3 Structural characteristics and the chemical composition of the 2-D InAs nanosheets grown with different indium fluxes

a In flux: 2.0×10^{-7} mbar

d	Composition (in at. %)	
Position	Ag	In
1	89.58	10.42
2	89.99	10.01
3	84.43	15.57

5 nm

b In flux: 4.9×10^{-7} mbar

e	Composition (in at. %)	
Position	Ag	In
1	52.70	47.30
2	98.14	1.86
3	70.81	29.19

5 nm

c In flux: 7.4×10^{-7} mbar

f	Composition (in at. %)	
Position	Ag	In
1	57.09	42.91
2	100	0
3	92.70	7.30

5 nm
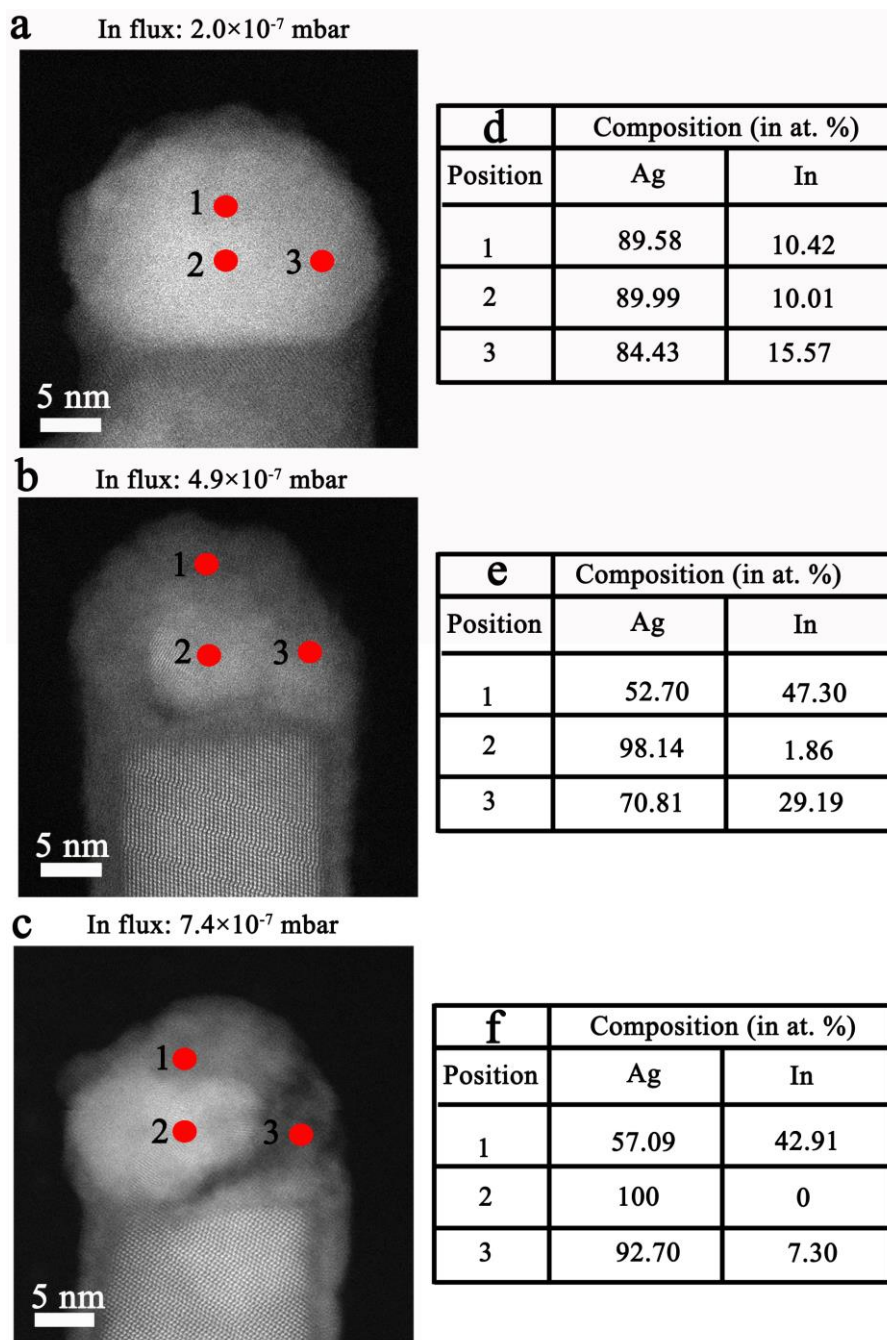
Figure S2. a-c, HAADF-STEM images taken from the InAs nanostructures grown with the indium flux of 2.0×10^{-7} mbar, 4.9×10^{-7} mbar and 7.4×10^{-7} mbar, respectively. **d-f**, Composition of silver and indium (in at. %) taken from the top region of the InAs nanowire (a), sheet-like structure (b) and nanosheet (c) by EDS point analysis. Red points in (a)-(c) highlight the positions where the EDS point analysis were recorded.

We find that the structural characteristic and the chemical composition of the catalyst alloy particle are strongly dependent on the indium flux. As shown in Fig. 2 in the main text, samples transform from 1-D nanowires to 2-D nanosheets with the indium flux increasing from 2.0×10^{-7} mbar to 7.4×10^{-7} mbar. For 1-D InAs nanowires, the spherical catalyst alloy particle is single-crystal and the elemental distributions of

silver and indium are already a little bit inhomogeneous comparing with the samples we grown with lower indium flux. When the morphology of InAs evolves from 1-D nanowire to 2-D nanosheet, the catalyst alloy particle transforms from single-crystal to polycrystalline, and the distribution of the silver atoms becomes more and more inhomogeneous with increasing indium flux. Figure S2 shows the composition of silver and indium (in at. %) taken from the top region of the InAs nanowire (Fig. S2a), sheet-like structure (Fig. S2b) and nanosheet (Fig. S2c) by EDS point analysis. As shown in Fig. S2d, a little bit inhomogeneous of distributions of silver and indium can be found, which is consistent with the EDS maps and line scan results in Fig. 2 in the main text. In Fig. S2e, EDS point analysis results confirm that the distribution of the silver and indium atoms becomes inhomogeneous. The atomic content of silver is up to 98.14% in the bright area of the seed particle (point 2), which is much higher than that in the similar area in the seed particle of nanowire. As shown in Fig. S2f, the inhomogeneous distribution of the silver atoms in catalyst alloy particle indeed becomes more obviously. The atomic content of silver is as high as 100% in the bright area of the seed particle (point 2), indicating pure silver nanoparticle segregates from the catalyst alloy particle of InAs. A dozen such EDS point analysis taken from the bright area of the seed particle revealed a 100% pure silver composition (there are some holes in the EDS map of indium element, where indium element could not be identified by EDS point analysis). For EDS point analysis, very low arsenic background (not shown here) can be detected because all our sample growth was terminated by switching off the indium supply while maintaining the arsenic supply until the substrate was cooled down below $300\,^{0}C$ within a few minutes.
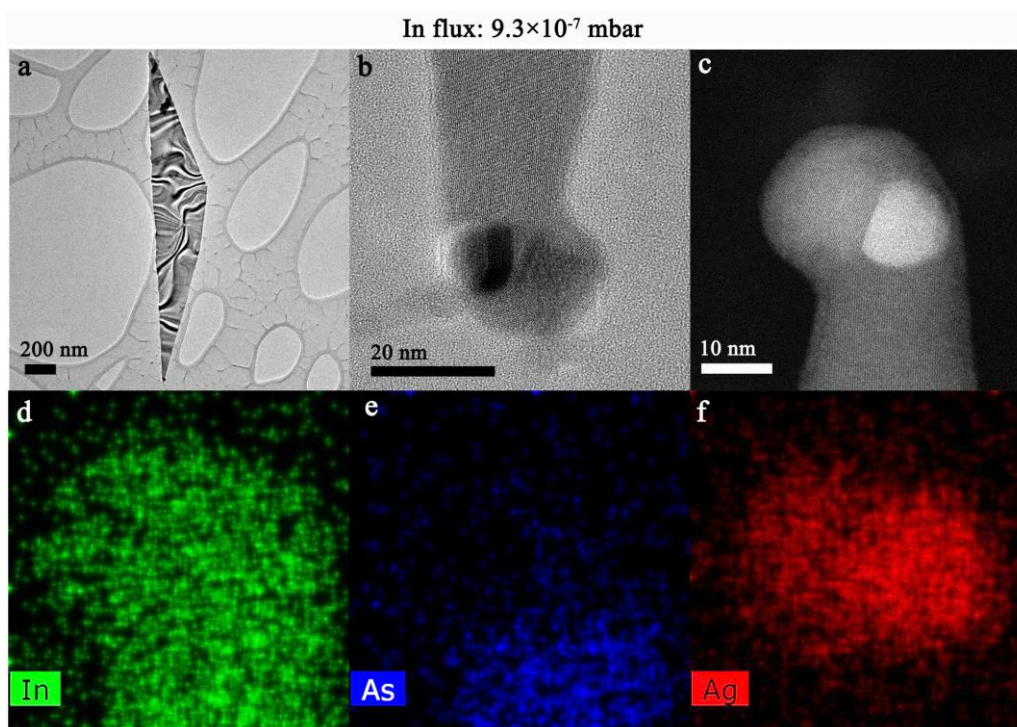
Figure S3. a-c, TEM, high-resolution TEM and HAADF-STEM images taken from an InAs nanosheet grown with the indium flux of 9.3×10^{-7} mbar, respectively. **d-f**, False-color EDS elemental maps taken at the top region of the InAs nanosheet in (c).

In fact, silver nanoparticle segregation from the catalyst alloy particle can be observed more clearly in the samples grown with higher indium flux. As shown in Fig. S3, when we further increasing the indium flux up to 9.3×10^{-7} mbar, we can see that

the size of the InAs nanosheets increase obviously (Fig. S3a). Interestingly, the silver nanoparticle which segregated from the catalyst alloy particle can be clearly observed from the TEM and STEM image (Fig. S3b,c). False-color EDS elemental maps (Fig. S3d-f) and EDS point analysis taken at the top region of the InAs nanosheet further confirm that silver segregates from the catalyst alloy.

S4 Unstable silver-indium alloy droplets
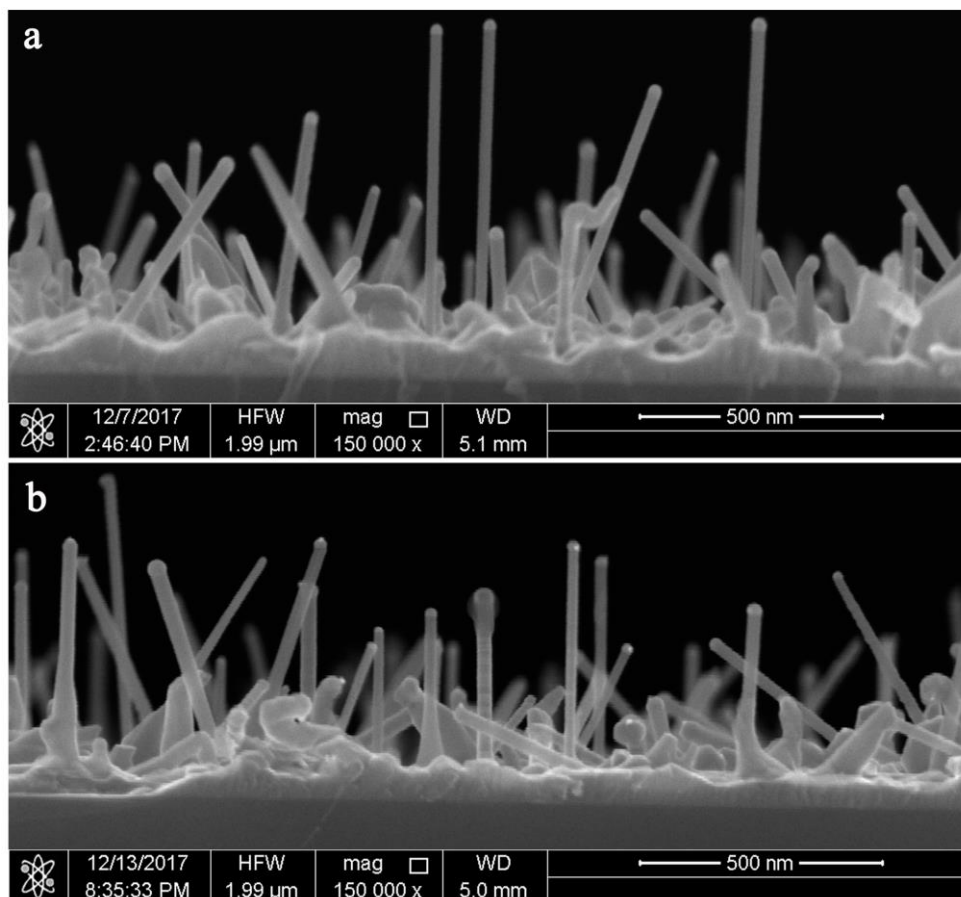
Figure S4. Side-view SEM images of InAs grown at indium-rich condition (indium flux: 9.3×10^{-7} mbar, arsenic flux: 5.9×10^{-6} mbar) on Si (111) substrates using silver as catalysts for 5 min at 505 ^{0}C. **a** and **b**, the same sample measured under the same condition with the time interval of one week, respectively. Silver nanoparticles segregated from the catalyst alloy can be observed directly from SEM images.

As we mentioned in the main text, the silver-indium alloy is unstable when the InAs samples grown under indium-rich condition. The unstable droplets will result in the silver nanoparticles segregating from the catalyst alloy spontaneously. Figure S4a is side-view SEM images of InAs grown under indium-rich condition (indium flux: 9.3×10^{-7} mbar, arsenic flux: 5.9×10^{-6} mbar) on Si (111) substrates using silver as catalysts with the growth time of 5 min and the growth temperature of 505 ^{0}C. We can see InAs nanowires forming and spherical catalyst alloy particles at the end of the InAs can be clearly observed. One week later, the same sample was measured under the same condition. Interestingly, small new nanoparticles can be found on the surface of the catalyst alloy particles, as shown in Fig. S4b. As can be seen from Fig. S5a,b, the small new nanoparticles can also be clearly observed from the HAADF-STEM

and high-resolution TEM images. Detailed EDS point analysis indicates the segregated nanoparticle is pure silver (Fig. S5c), which is consist with the results in Figs. S2 and S3.

c	Composition (in at. %)	
Position	Ag	In
1	100	0
2	100	0
3	100	0
4	89.96	10.04
5	88.73	11.27
6	91.45	8.55
7	89.68	10.32
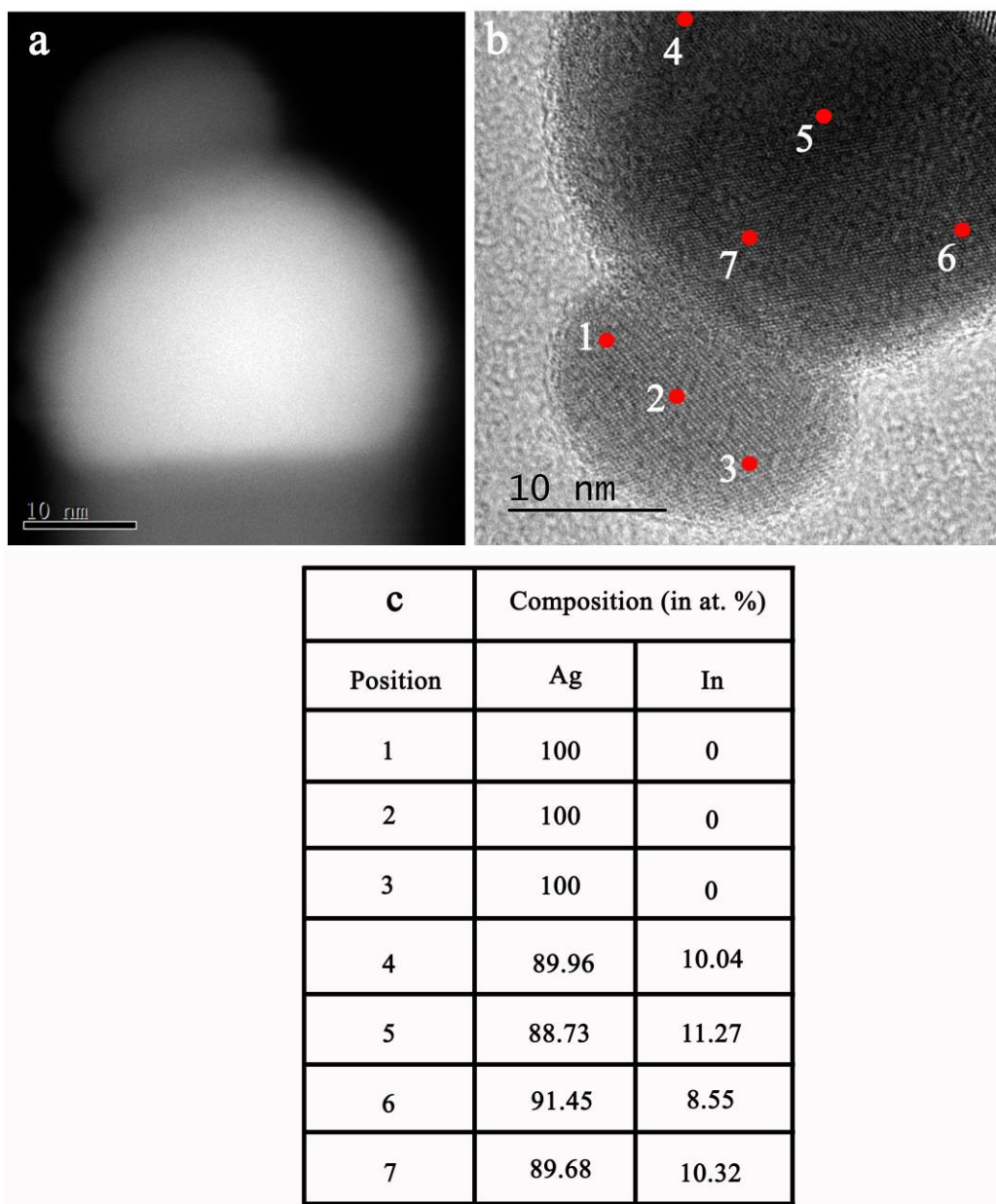
Figure S5. a,b, HAADF-STEM and high-resolution TEM images taken from the top section of an InAs nanowire in Fig. S4b, respectively. **c**, Composition of silver and indium (in at. %) taken from the top region of the InAs nanowire (b) by EDS point analysis. Red points in (b) highlight the positions where the EDS point analysis were recorded.

S5 InAs samples grown under the same indium-rich growth condition for different growth time

In Table S2, we have summarized the growth parameters for the InAs samples grown under the same indium-rich growth condition with different growth time in Fig. 3a-f in the main text.

Table S2. Summary of growth parameters for the InAs samples grown with different time.

Substrates	Series	Indium flux (mbar)	Arsenic flux (mbar)	V/III	Growth time (min)	Growth temperature (℃)
Si (111)	Variant growth time	9.3×10^{-7}	5.9×10^{-6}	6.3	**2.5**	505
		9.3×10^{-7}	5.9×10^{-6}	6.3	**5**	505
		9.3×10^{-7}	5.9×10^{-6}	6.3	**10**	505
		9.3×10^{-7}	5.9×10^{-6}	6.3	**15**	505
		9.3×10^{-7}	5.9×10^{-6}	6.3	**40**	505
		9.3×10^{-7}	5.9×10^{-6}	6.3	**80**	505

Figure S6 shows SEM images of the 2-D InAs nanosheets grown at indium-rich condition (indium flux: 9.3×10^{-7} mbar, arsenic flux: 5.9×10^{-6} mbar) on Si (111) substrates using silver as catalysts with the growth time of 40 min and the growth temperature of 505 ^{0}C. Larger-scale high density free-standing 2-D nanosheets have been obtained on the Si (111) substrate.
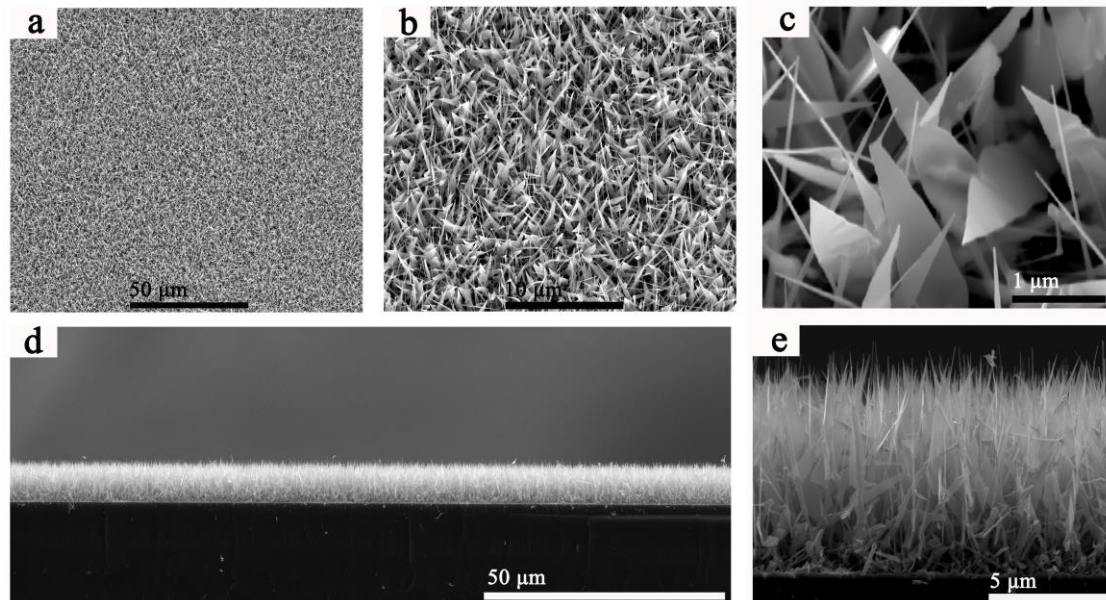
Figure S6. 25° tilted (**a-c**) and side view (**d,e**) SEM images of 2-D InAs nanosheets grown at indium-rich condition (indium flux: 9.3×10^{-7} mbar, arsenic flux: 5.9×10^{-6} mbar) on Si (111) substrates using silver as catalysts for 40 min at 505 ^{0}C. **b** and **c** are magnified SEM images of (a), and **e** is magnified SEM image of (d).

S6 Structural characteristics and the chemical composition of the InAs nanostructures grown under the same indium-rich growth condition for different growth time
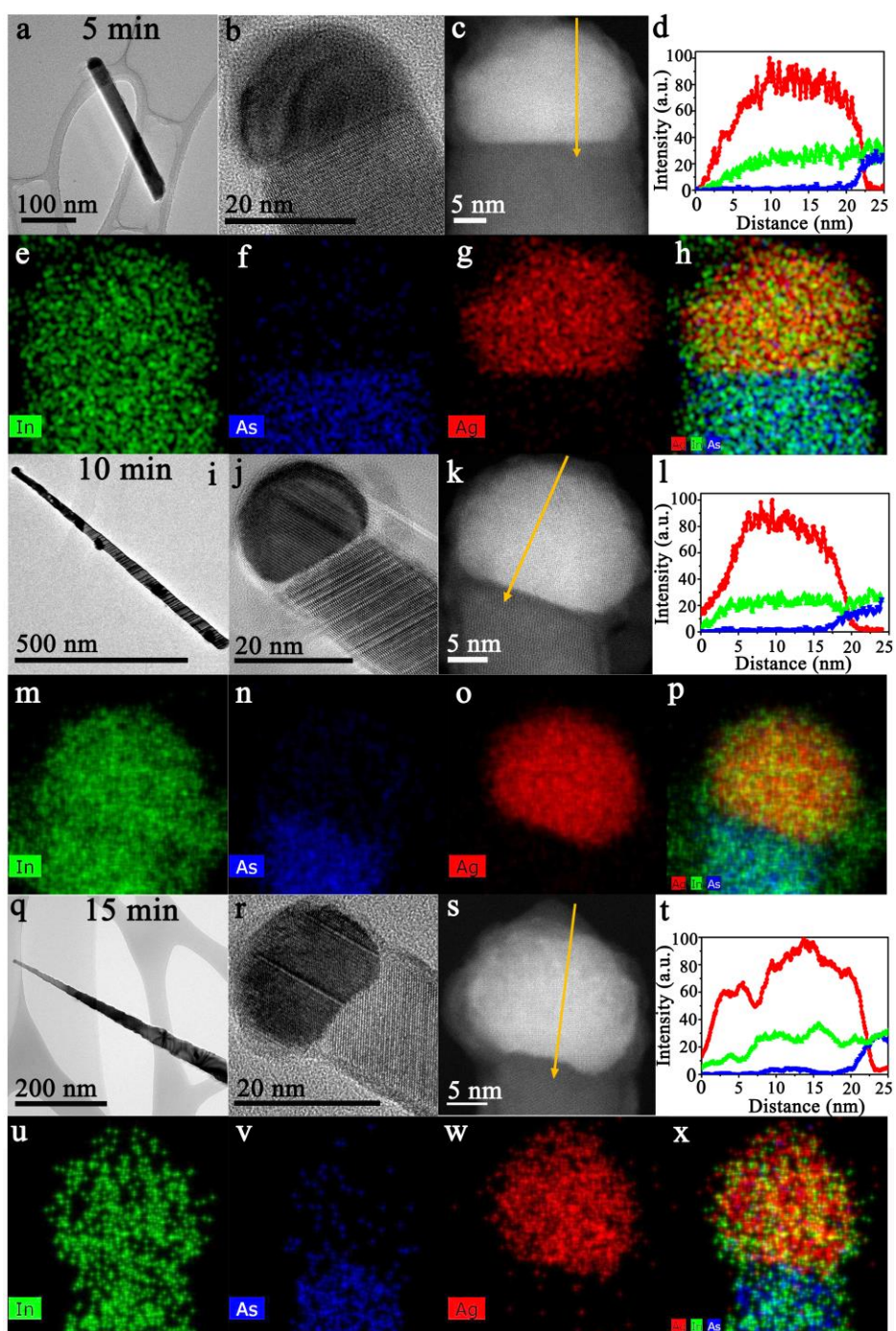
Figure S7. Crystal structure and elemental distribution of catalyst alloy particle of the InAs grown at indium-rich condition (indium flux: 9.3×10^{-7} mbar, As flux: 5.9×10^{-6} mbar) on Si (111) substrates for different growth time. **a-c**, **i-k**, **q-s**, TEM, high-resolution TEM and HAADF-STEM images taken from the InAs nanostructures grown for 5 min, 10 min and 15 min, respectively. **e-h**, **m-p**, **u-x**, False-color EDS elemental maps taken at the top region of the InAs nanostructures in (c), (k) and (s), respectively. **d**, **l**, **t**, EDS line scans taken along the axial direction (marked with yellow arrows) of the catalyst alloy particle in (c), (k) and (s), respectively.

10

d	Composition (in at. %)	
Position	Ag	In
1	91.80	8.20
2	97.97	2.03
3	92.97	7.03
4	91.23	8.77
5	92.66	7.34
6	92.43	7.57

e	Composition (in at. %)	
Position	Ag	In
1	93.75	6.25
2	91.11	8.89
3	87.49	12.51
4	95.34	4.66
5	95.93	4.07
6	89.86	10.14

f	Composition (in at. %)	
Position	Ag	In
1	100	0
2	88.43	11.57
3	80.91	19.09
4	100	0
5	95.90	4.10
6	82.30	17.70
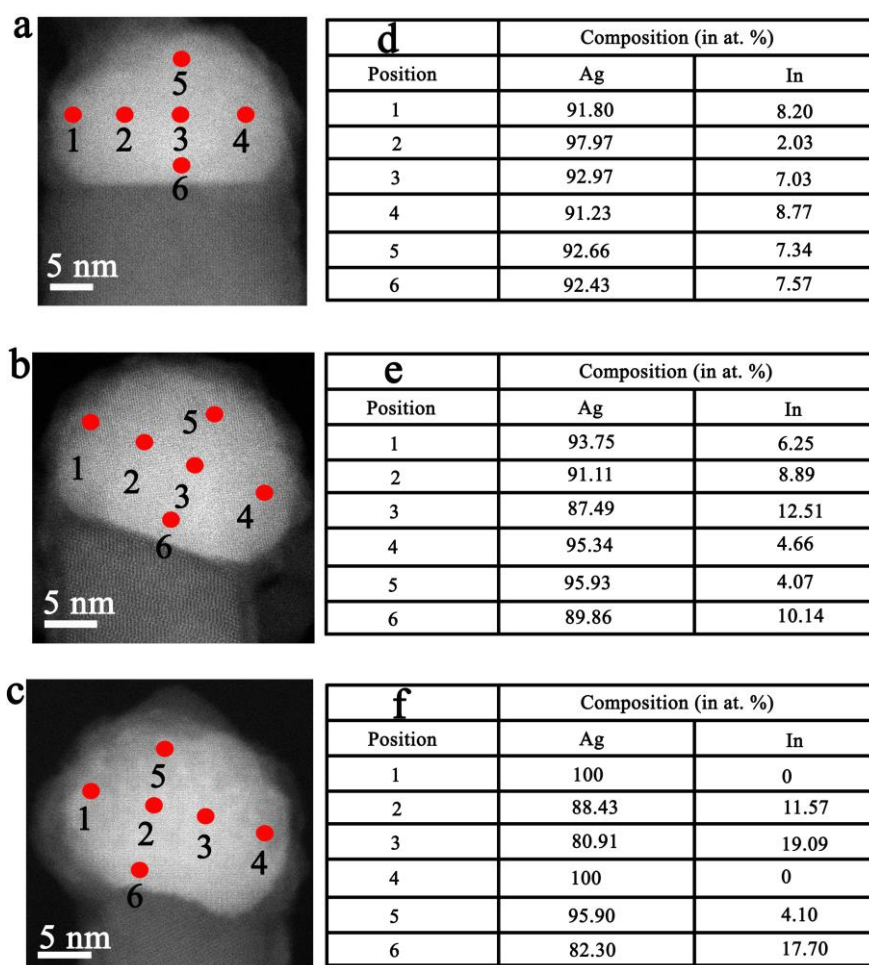
Figure S8. a-c, HAADF-STEM images taken from the InAs grown at indium-rich condition (indium flux: 9.3×10^{-7} mbar, arsenic flux: 5.9×10^{-6} mbar) on Si (111) substrates for 5 min, 10 min and 15 min, respectively. **d-f**, Composition of silver and indium (in at. %) taken from the top region of the InAs nanowire (a), sheet-like structure (b) and nanosheet (c) by EDS point analysis. Red points in (a)-(c) highlight the positions where the EDS point analysis were recorded.

To observe the catalyst alloy segregation process, detailed TEM, HAADF-STEM and EDS measurements have been carried out on the InAs nanostructures grown under the same indium-rich growth condition for different time. When the growth time is 5 min, TEM results further confirm that the morphology of the sample is 1-D nanowire. As can be seen from Fig. S7a, the InAs nanowire has a homogeneous diameter, and a spherical catalyst alloy particle at the end of the InAs can be clearly observed. High-resolution TEM and HAADF-STEM images of the spherical catalyst alloy particle indicate that the alloy particle is fully single-crystalline (Fig. S7b,c). EDS maps (Fig. S7e-h), line scan (Fig. S7d) and point analysis (Fig. S8d) taken at the top region of the InAs nanowire indicate that the remaining spherical catalyst particle is composed of silver and indium. The elemental distributions of silver and indium are already a little bit inhomogeneous since the sample grown under an indium-rich condition. As shown in Fig. S7i, increasing the growth time to 10 min, lateral growth of InAs appears, which is consist with the SEM image in Fig. 3c in the main text. It is noteworthy that the spherical catalyst alloy particle is not a perfect single-crystal any more according to the high-resolution TEM result in Fig. S7j. EDS maps (Fig. S7m-p), line scan (Fig. S7l) and point analysis (Fig. S8e) taken at the top region of the InAs

further indicate that the distribution of the silver atoms becomes inhomogeneous. Figure S7q is a typical TEM image of an InAs sample grown for 15 min, and InAs has a sheet-like morphology. From the high-resolution TEM and HAADF-STEM images in Fig. S7r,s, we can see that more defects in the catalyst alloy particle appear. The inhomogeneous distribution of the silver atoms in catalyst alloy particle is very obvious, which can be confirmed by EDS maps (Fig. S7u-x), the line scan (Fig. S7t) and point analysis (Fig. S8f). For example, there are some holes in the EDS map of indium element (Fig. S7u), and thus atomic content with 100% silver can be obtained from the EDS point results (Fig. S8f). Further increasing the growth time to 40 min and longer, the pure silver nanoparticle segregates from the catalyst alloy particle of InAs, and it can be clearly observed and detected from the STEM images and EDS point analysis (not shown here), as that observed in Fig. 2 in the main text and Fig. S3. Other phenomena observed in the samples grown with different indium fluxes are also observed in these samples. That is, the interface shape between catalyst and InAs varies from linear to curve gradually (Fig. S7c,k,s) with increasing the growth time. Thin indium shells can also be observed on the surface of catalyst alloy particles and InAs, which once again confirm that the indium-rich condition plays an important role in the dimensional transformation for InAs (Fig. S7h,p,x). With increasing the indium flux in Fig. 2 in the main text, the growth condition will be indium-rich gradually; With increasing the growth time for samples grown in the same indium-rich condition, the growth condition will also be indium-rich more and more. Both of them are very helpful for the catalyst alloy segregation and that is why very similar dimensional transformation is observed in these two series of samples.

S7 Transformation process of InAs from a 1-D nanowire to 3-D complex nanocrosses

In the main text (Fig. 3g-o), we described the catalyst alloy segregation process for the dimensions of InAs transform from 1-D to 2-D (The segregated silver droplets seed new InAs nanowire growth on the substrate surface). We find that transformation process of InAs from a 1-D nanowire to 3-D complex nanocrosses can also be achieved, when the segregated silver droplets seed new InAs nanowire growth on the nanosheet facet under an indium-rich condition. Figure S9 is schematic demonstration of the catalyst alloy segregation process for the evolution of the InAs from the 1-D nanowire to the 3-D complex nanocrosses. New InAs nanowires seeded by the segregated silver droplets can be directly observed by SEM. Figure S10 shows side-view SEM images of InAs grown at indium-rich condition (indium flux: 9.3×10^{-7} mbar, arsenic flux: 5.9×10^{-6} mbar) on Si (111) substrates using silver as catalysts for 40 min at 505 ^{0}C. As shown in Fig. S10a,b (red rectangles regions), the new InAs nanowires indeed can be found on the side wall of the 2-D nanosheets. Figure S11 (also in Fig. 1h in the main text) shows a TEM image of the 3-D complex InAs nanocrosses grown at indium-rich condition (indium flux: 1.0×10^{-6} mbar, arsenic flux: 5.9×10^{-6} mbar) on Si (111) substrates using silver as catalysts for 40 min at 505 ^{0}C. We can see that the 3-D nanocrosses consist of a double 2-D nanosheets cross and a 1-D nanowire/2-D nanosheet cross.
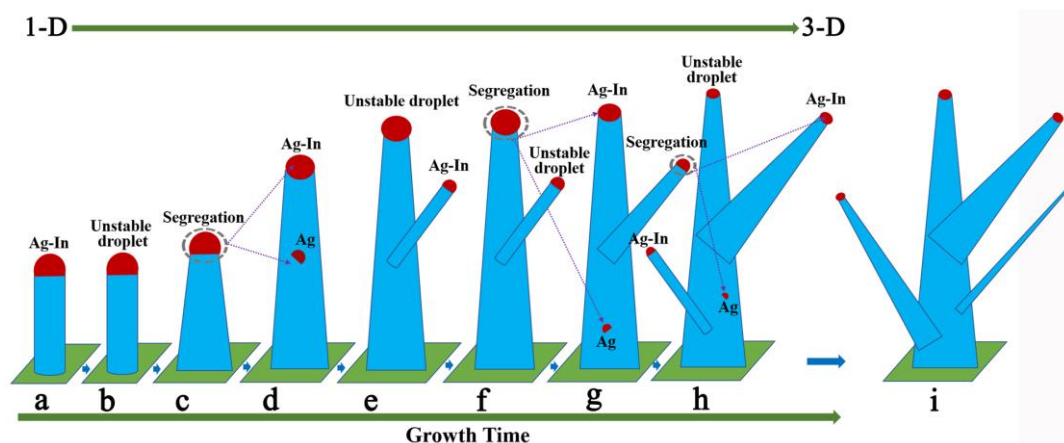
Figure S9. Schematic demonstration of the catalyst alloy segregation process for the evolution of the InAs from a 1-D nanowire to 3-D complex nanocrosses under an indium-rich condition. **a**, An InAs nanowire with a spherical silver-indium alloy droplet on its top. **b**, Silver-indium alloy droplet becomes unstable under an indium-rich growth condition. **c**, Silver-indium alloy droplet starts segregation and the morphology of InAs evolves from 1-D nanowire to 2-D nanosheet gradually. **d**, Silver-indium alloy droplet finishes segregation and the segregated silver droplet in (c) migrates to the nanosheet side wall. **e**, Silver-indium alloy droplet on the 2-D nanosheet becomes unstable, and the segregated silver droplet seeds a new InAs nanowire growth on the facet of the nanosheet. **f**, Silver-indium alloy droplet on the 2-D nanosheet starts segregation again, and silver-indium alloy droplet on the new 1-D InAs nanowire becomes unstable. **g**, Silver-indium alloy droplet on the 2-D nanosheet finishes segregation and the segregated silver droplet in (f) migrates to the facet of the nanosheet. Silver-indium alloy droplet on the new 1-D InAs nanowire starts segregation and the morphology of the new InAs evolves from 1-D nanowire to 2-D nanosheet gradually. **h**, Silver-indium alloy droplets undergo the same segregation process in (a)-(g); **i**, An illustration of one kind of 3-D complex nanocrosses obtained by continue catalyst alloy segregation.
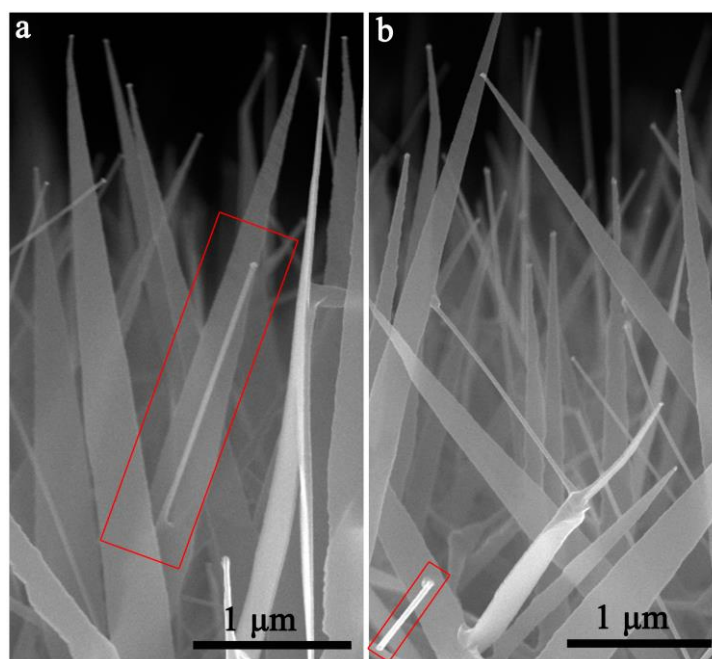
Figure S10. a,**b**, Side-view SEM images of InAs grown at indium-rich condition (indium flux: 9.3×10^{-7} mbar, arsenic flux: 5.9×10^{-6} mbar) on Si (111) substrates using silver as catalysts for 40 min at 505 ^{0}C. The red rectangles highlight the regions where the segregated silver droplet seeds new InAs nanowire growth on the facet of the nanosheet.
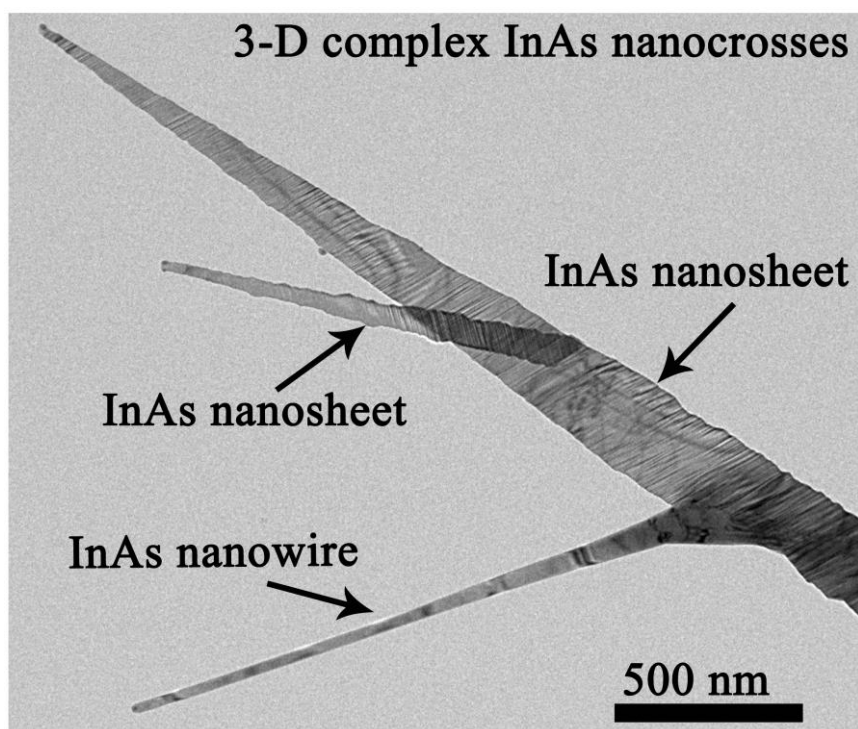
Figure S11. TEM image of the 3-D complex InAs nanocrosses grown at indium-rich condition (indium flux: 1.0×10^{-6} mbar, arsenic flux: 5.9×10^{-6} mbar) on Si (111) substrates using silver as catalysts for 40 min at 505 ^{0}C.
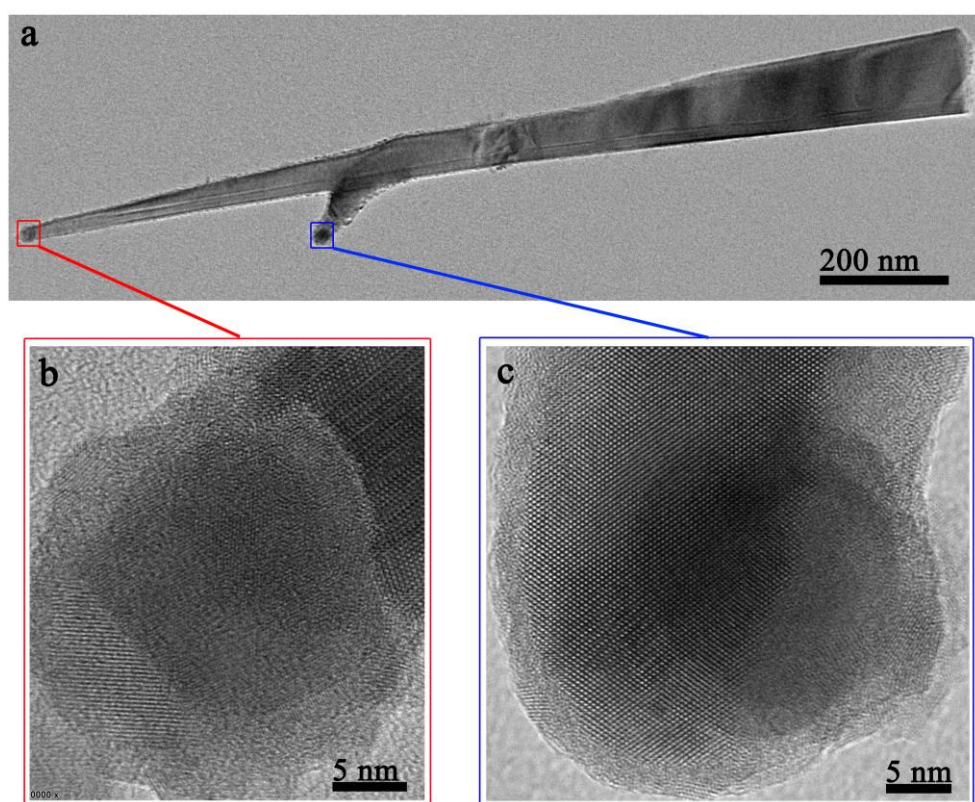
Figure S12. a, TEM image of a 2-D InAs nanosheet cross grown at indium-rich condition (indium flux: 1.0×10^{-6} mbar, arsenic flux: 5.9×10^{-6} mbar) on Si (111) substrates using silver as catalysts for 40 min at 505 ^{0}C. **b,c**, High-resolution TEM images taken from the top section of the two nanosheets.

Figure S12a shows a TEM image of a 2-D InAs nanosheet cross grown at indium-rich condition (indium flux: 1.0×10^{-6} mbar, arsenic flux: 5.9×10^{-6} mbar) on Si (111) substrates using silver as catalysts for 40 min at 505 ^{0}C. In Figure S12b,c, catalyst alloy droplets can be clearly observed. EDS point analysis indicates that both of them are composed of silver and indium.

S8 Possible growth mechanism of the 2-D InAs nanosheets

In our work, the growth mechanism of InAs nanostructures is growth parameter (here is indium flux) dependent. According to our previous work[3] and the results in this paper, InAs grown with a high V/III BEP ratio (low indium flux and indium-poor growth condition) is 1-D nanowires. The composition for the catalyst particles on these nanowires was found to range from ~13 to ~25 at. % indium. The silver-indium alloy phase diagram shown in Fig. S13 indicates that stable phases within these indium compositions are silver and Ag$_3$In. The melting points ($T_m \approx 860$ °C at 13 at. % indium and $T_m \approx 740$ °C at 25 at. % indium) and eutectic temperature (695 °C) of them are higher than all the nanowire growth temperatures. Therefore, the catalyst possibly has solid state during nanowire growth as reported in Au-seeded InAs nanowires[4]. That is to say, the growth of InAs nanowires is governed by the vapor-solid-solid (VSS) process. In Fig. S14, we have provided the schematic demonstration of the possible growth mechanisms for the dimensional evolution of InAs from 1-D to 2-D under the same indium-rich condition for different time. When the growth locates at the initial stage (the value of indium flux is smaller than that can produce an unstable droplet, as shown in Fig. 3a in the main text), InAs is still 1-D nanowires and the nanowires can keep the VSS growth (Fig. S14a). As shown in Fig. S14b, when the growth atmosphere of InAs is gradually becoming indium-rich with increasing the growth time, the silver-indium alloy droplet will become unstable and the distribution of the silver atoms becomes inhomogeneous (Fig. 3h in the main text). EDS results show that indium composition in catalyst particles can reach ~50 at. % (liquid phase silver-indium alloy at sample growth temperature), indicating that the vapor-solid-liquid (VLS) process begins to appear. As soon as the indium-rich growth condition reaches, the silver-indium alloy droplet starts segregation and the growth is governed by the VSS and VLS mechanisms simultaneously (Fig. S14c), and the morphology of InAs evolves from 1-D nanowire to 2-D nanosheet gradually due to the anisotropical growth caused by catalyst alloy segregation (the exact anisotropical growth process needs further investigation with an *in situ* TEM, which will be presented later). Next, after the silver-indium alloy finishes the silver segregation, the growth of InAs is governed by the VSS process again (indium composition in catalyst particles is similar with that in the catalyst alloy of nanowires, and we conjecture that the excessive indium atoms form an indium shell around the nanosheet) until the silver-indium alloy droplet become unstable once again (Fig. S14d,e). With the continuation of the growth, the growth mechanisms repeat VSS-(VSS+VLS)-VSS (Fig. S14e-i) until the catalyst alloy segregation is stopped due to the too small size of the catalyst alloy particle.
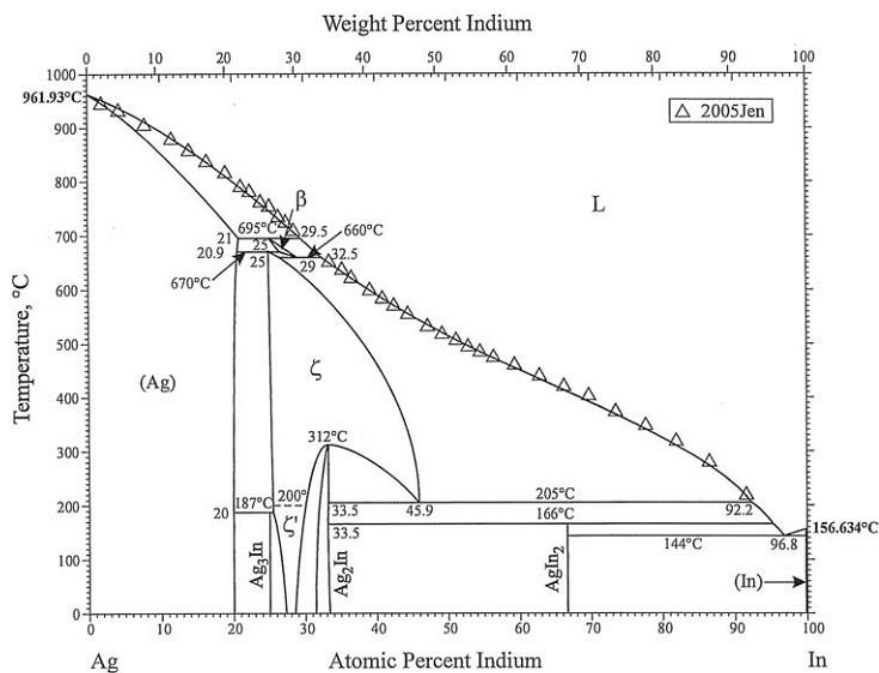
Figure S13: Ag-In phase diagram (Okamoto, H. J. Phase Equilib. Diffus. 27 (2006) 535).
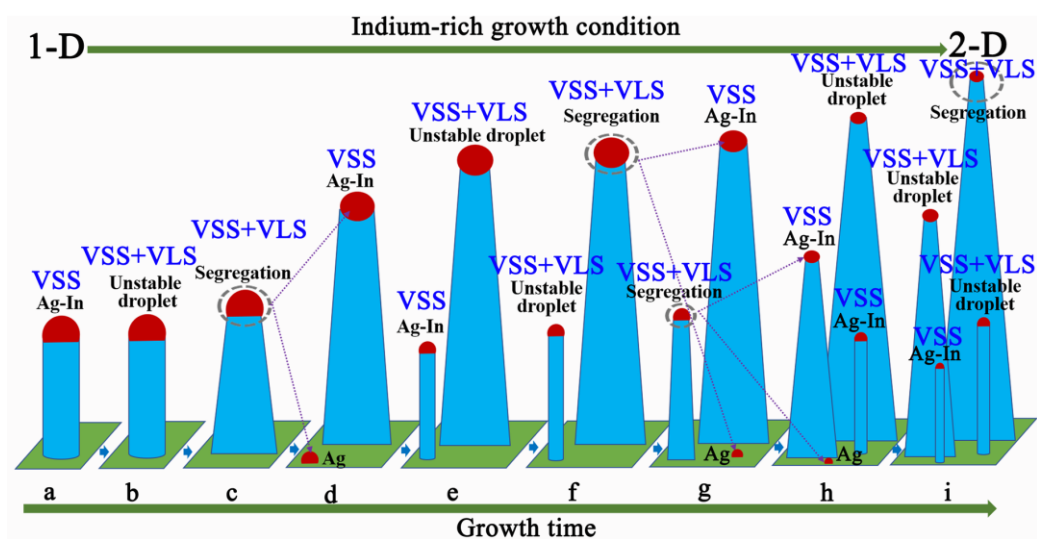
Figure S14: Schematic demonstration of the possible growth mechanisms for the dimensional evolution of InAs from 1-D to 2-D under the same indium-rich condition with different growth time.

One previous work[5] has provided lots of valuable information for us to understand our observations in our study. During the MBE growth, only the growth species were introduced in the growth chamber, hence the V/III BEP ratio can be used to determine the partial pressure of each growth species. Therefore, with a low V/III BEP ratio (arsenic-limited), the indium vapor partial pressure in the growth chamber should be relatively increased. Under this situation, almost all silver catalysts can absorb more indium, resulting in a high supersaturation in the catalysts. The increased catalyst supersaturation should accelerate the axial nanosheet growth. This is consistent with our observations (the average axial growth rate for 1-D nanowires is 75 nm/min, while for 2-D nanosheets it is 200 nm/min), suggesting that the indium concentration

in the catalysts indeed is the dominating factor for InAs nanosheet growth in our case. It has been well documented that high supersaturation in the catalyst can promote the formation of wurtzite (WZ) structure, whereas low supersaturation is favored for the generation of zinc-blende (ZB) structure[6]. Therefore, 2-D InAs nanosheets with high catalyst supersaturation tend to nucleate in WZ structure, and this is consistent with our TEM observations. That is, almost all the InAs nanosheets have WZ structure (few nanosheets have ZB structure, which is growth direction dependent).

A very difficult thing for us to understand is that the physical mechanisms of the silver segregates from the silver-indium alloy for our samples grown under indium-rich condition. To find out a possible solution for this problem, theoretical analysis of silver segregation mechanism has been carried out.

Segregation refers to the enrichment of atoms, ions or molecules at a microscopic region in an alloy system[7]. Chemical potential, as a kind of driving forces, plays an important role in many chemical equilibriums or in phase equilibriums[8]. In an alloy material system, while the chemical potential of metal cations is larger than that of its elementary substance, these cations will precipitate out of the material and convert into elemental metal. It is reasonable to assume that the chemical potential change near the phase transition boundary ((Ag) $\to$ (Ag)+Ag$_3$In) drives the segregation of silver. We calculated the chemical potential of two phase on both sides of the phase transition boundary. The ground state structures of two phase (Ag$_4$In and Ag$_3$In) are gained by using cluster expansion approach as implemented in the Alloy-Theoretic Automated Toolkit[9]. We found that the calculated chemical potential difference of silver in Ag$_3$In is always larger than that of silver in Ag$_4$In, lacking an intersection throughout the chemical potential domain (Fig. S15a). So, the chemical potential cannot explain the segregation phenomenon we observed.
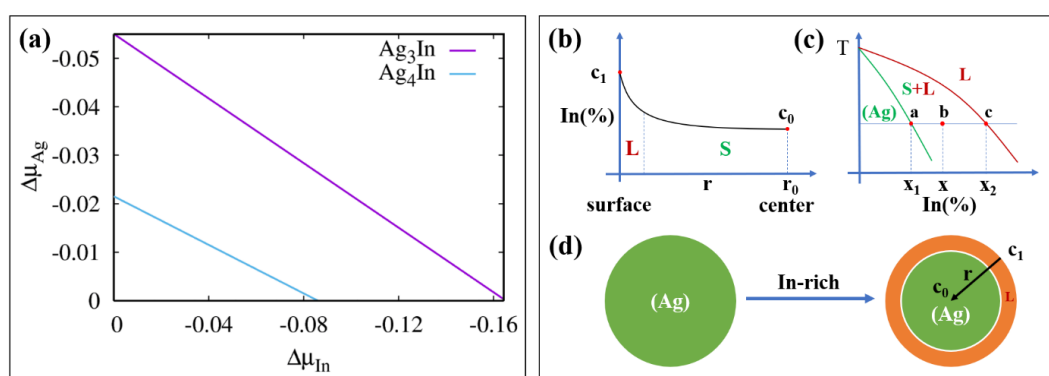
Figure S15. Theoretical analysis of silver segregation mechanism. **a**, Calculated chemical potential at phase transition boundary ((Ag) $\to$ (Ag)+Ag$_3$In). Right hand side panels demonstrate the possible mechanism of silver segregation. **b**, Concentration distribution of indium in Ag-In catalyst particle. **c**, Concentration of indium (x_1 and x_2) in the solid and liquid phases when alloy locates in two-phase region. **d**, Schematic diagram of Ag-In alloy particle liquefaction in indium-rich environment.

Experimentally, with increasing indium flux, we observed that catalyst alloy particles firstly liquify and then segregate. It implies here that solid and liquid phases coexist. It is well-known that the compositions between the solid and liquid phases exist discrepancy when alloy locates in two-phase coexistence zone. In this case, solute redistribution determines phase distribution as well as concentration segregation[10]. Through deliberate analysis, we found that solute redistribution may be used to explain the segregation phenomenon in the experiment. The possible mechanism is as follows:

1. During MBE growth process, indium diffuses into the interior of the catalyst particles through their surfaces. Here, it exists a concentration gradient along the radius of the spherical catalyst particles (Fig. S15b). When the flux rate of indium is increased to a certain extent, the concentration of indium on the catalyst surface exceeds the upper limit of solid solution and enters the liquid phase zone. Sequentially, the atoms on the surface begin to melt (Fig. S15d).

2. According to the Ag-In phase diagram[11], the concentration of indium in liquid phase is much larger than that in solid phase (see Fig. S15c). As the atoms on the catalyst surface melt, indium atoms trend to diffuse from the solid phase into the liquid phase.

3. The solid-state catalyst particles slip down to the substrate under the liquid wetting and gravity. These fallen catalysts will continue to catalyze the growth of new InAs nanowires.

4. After several cycles of 1-3 steps, indium in catalyst particles can be almost completely removed and distributed in the liquid. This process is very similar to the zone melting invented by John Desmond Bernal, which also utilizes solute redistribution to purify metal, i.e. electronic-grade silicon. Based on the Ag-In phase diagram, our estimated equilibrium partition ration (κ_0) is less than 0.3. Generally, if $\kappa_0 < 0.5$, it is very effective for removing impurities and purifying metals. For example, if $\kappa_0 < 0.1$, the zone melting method can reduce the concentration of impurities in the metals by three orders of magnitude through only five cycles.

At last, we would like to point out that in our work, we are limited to postgrowth investigations of the particle phases and composition, i.e. with *ex situ* characterization. Thus, the future work is required to further understand the exact mechanism of the catalyst alloy segregation as well as dimensional transformation of InAs nanostructures for indium-rich growth with more advanced methods. For example, with an *in situ* TEM, the particle composition could be monitored, starting with an indium-rich particle, and the exact moment and mechanism of the InAs dimensional transformation can be observed. Then, with by observing the particle phase *in situ*, comparison to kinetic modeling of the meta-stable phases would become extremely interesting.

S9 Information on the dimensional tunability of InAs from 1-D to 2-D using 'catalyst alloy segregation' with a two-step growth procedure

We find that the tuning the dimension of the low-dimensional III-V semiconductors by the catalyst alloy segregation is a general method. For example, we can realize the dimensional tunability of InAs from 1-D to 2-D using 'catalyst alloy segregation' with a two-step growth procedure. In the so-called two-step growth process, InAs nanowires are firstly grown on the substrate with silver as catalysts, and then tuning the growth conditions to 'indium-rich' (after InAs nanowire growth, increasing the indium flux to a large value and keeping other parameters constant) to ensure that the catalyst alloy segregation can happen.

Figure S16a-i is schematic demonstration of the dimensional tunability of InAs from 1-D to 2-D using 'catalyst alloy segregation' with a two-step growth procedure. As shown in Fig. S16c-i, once the catalyst alloy segregation happens, the morphology of InAs will evolve from 1-D nanowire to 2-D nanosheet with the same process described in Fig. 3g-o in the main text. In Table S3, we have summarized the growth parameters for the 2-D InAs nanosheets grown with this procedure. In the first step, the InAs nanowires were grown on the p-type Si (111) substrates with a V/III BEP ratio of 39.3 at 505 °C for 40 min; In the second step, the InAs nanowire growth was terminated by closing the indium source shutter and keeping the arsenic source shutter open. Following that, the indium flux was increased by increasing the indium source temperature to provide an indium-rich growth condition. Finally, the 2-D InAs nanosheets growth was initiated by opening the indium source shutter.

Table S3. Summary of growth parameters for the 2-D InAs sheets grown with a two-step growth procedure in the main text.

Substrates	Series	Procedure	Indium flux (mbar)	Arsenic flux (mbar)	V/III	Growth time (min)	Growth temperature (°C)
Si (111)	Two-step growth procedure	The first step	1.5×10^{-7}	5.9×10^{-6}	39.3	40	505
		The second step	4.9×10^{-7}	5.9×10^{-6}	12.0	60	505
			8.4×10^{-7}	5.9×10^{-6}	7.0	60	505
			4.9×10^{-7}	5.9×10^{-6}	12.0	60	525

To check the influence of indium flux on the morphology of the 2-D InAs nanosheets, two samples were grown with V/III BEP ratios (for the second step) of 12.0 (Fig. S16j) and 7.0 (Fig. S16k). To obtain the growth temperature window for the 2-D InAs nanosheets grown by the two-step growth procedure, samples have been grown at different substrate temperatures. Figure S16m-o shows the SEM images of the 2-D InAs nanosheets grown on the 1-D nanowires with the two-step growth procedure using different indium fluxes and growth temperatures. We can see from Fig. S16m,n that 2-D InAs nanosheets can be obtained with the V/III BEP ratios of 12.0 (Fig. S16m) and 7.0 (Fig. S16n). The density and size of the latter are obvious larger than the former owing to the larger indium flux used, which is consistent with

the results obtained directly on the Si substrates in Fig. 1 in the main text. As shown in Fig. S16o, 2-D InAs nanosheets can also be observed on the substrate for the sample grown at a higher temperature (525 °C, Fig. S16l).
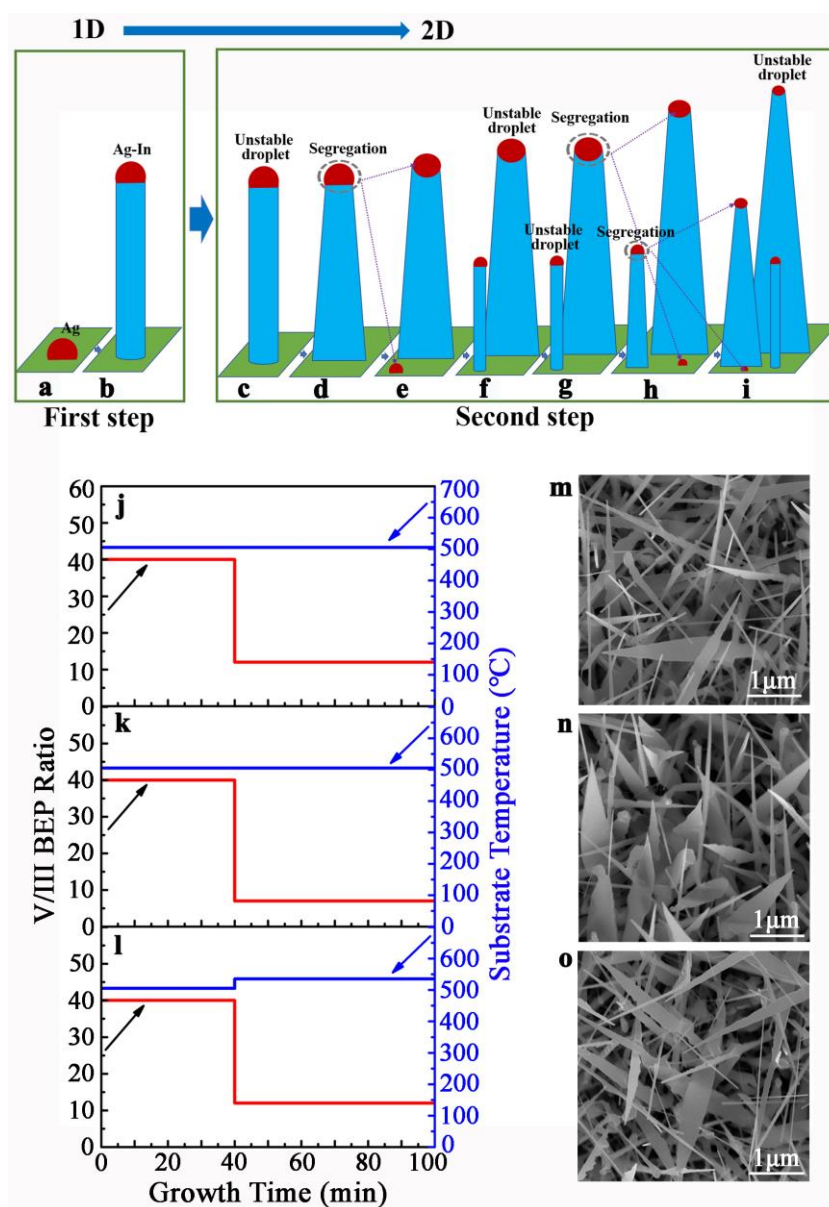
Figure S16. Schematic demonstration of the dimensional tunability of InAs from 1-D to 2-D using 'catalyst alloy segregation' with a two-step growth procedure and the corresponding experimental results. First step: the 1-D InAs nanowire growth. **a**, Silver nanoparticle forms on the substrate surface. **b**, Silver nanoparticle seeds InAs nanowire growth. Second step: After the 1-D InAs nanowire growth, keeping the arsenic flux constant and increasing the indium flux, the 2-D InAs nanosheet grown under an indium-rich growth condition with 'catalyst alloy segregation'. **c**, Silver-indium alloy droplet becomes unstable under an indium-rich growth condition. **d**, Silver-indium alloy droplet starts segregation and the morphology of InAs evolves from 1-D nanowire to 2-D nanosheet gradually. **e**, Silver-indium alloy droplet finishes segregation and the segregated silver droplet in **d** migrates to the substrate surface. **f**, Silver-indium alloy droplet on the 2-D nanosheet becomes unstable and the segregated silver droplet seeds a new InAs nanowire growth. **g**, Silver-indium alloy droplet on the 2-D nanosheet starts segregation again and silver-indium alloy droplet on the new 1-D InAs nanowire becomes unstable. **h,i**, Silver-indium alloy droplets undergo the same segregation process in **c-g** and Fig. 3g-m in the main text and high

density 2-D InAs nanosheets form on the substrate. **h-l**, Detailed growth conditions for the 2-D InAs nanosheet grown with the two-step growth procedure. **m-o**, 25° tilted SEM images of the 2-D InAs nanosheets grown with the two-step growth procedure. In the first step, all the InAs nanowires are grown with a V/III BEP ratio of 39.3 (indium and arsenic fluxes are 1.5×10^{-7} mbar and 5.9×10^{-6} mbar, respectively) for 40 min at 505 °C. In the second step, indium fluxes are 4.9×10^{-7} mbar (j), 8.4×10^{-7} mbar (k), and 4.9×10^{-7} mbar (l), and corresponding growth temperatures are 505 °C (j), 505 °C (k) and 525 °C (l); samples are all grown for 60 min.

a

Substrate	Procedure	In flux (mbar)	As flux (mbar)	V/III	Growth time (min)	Growth temperature (°C)
P-Si(111)	The first step	1.5×10^{-7}	5.9×10^{-6}	39.3	10	505
	The second step	8.4×10^{-7}	5.9×10^{-6}	7.0	60	505

b

c

d

Substrate	Procedure	In flux (mbar)	As flux (mbar)	V/III	Growth time (min)	Growth temperature (°C)
P-Si(111)	The first step	1.5×10^{-7}	5.9×10^{-6}	39.3	15	505
	The second step	8.4×10^{-7}	5.9×10^{-6}	7.0	60	505

e

f
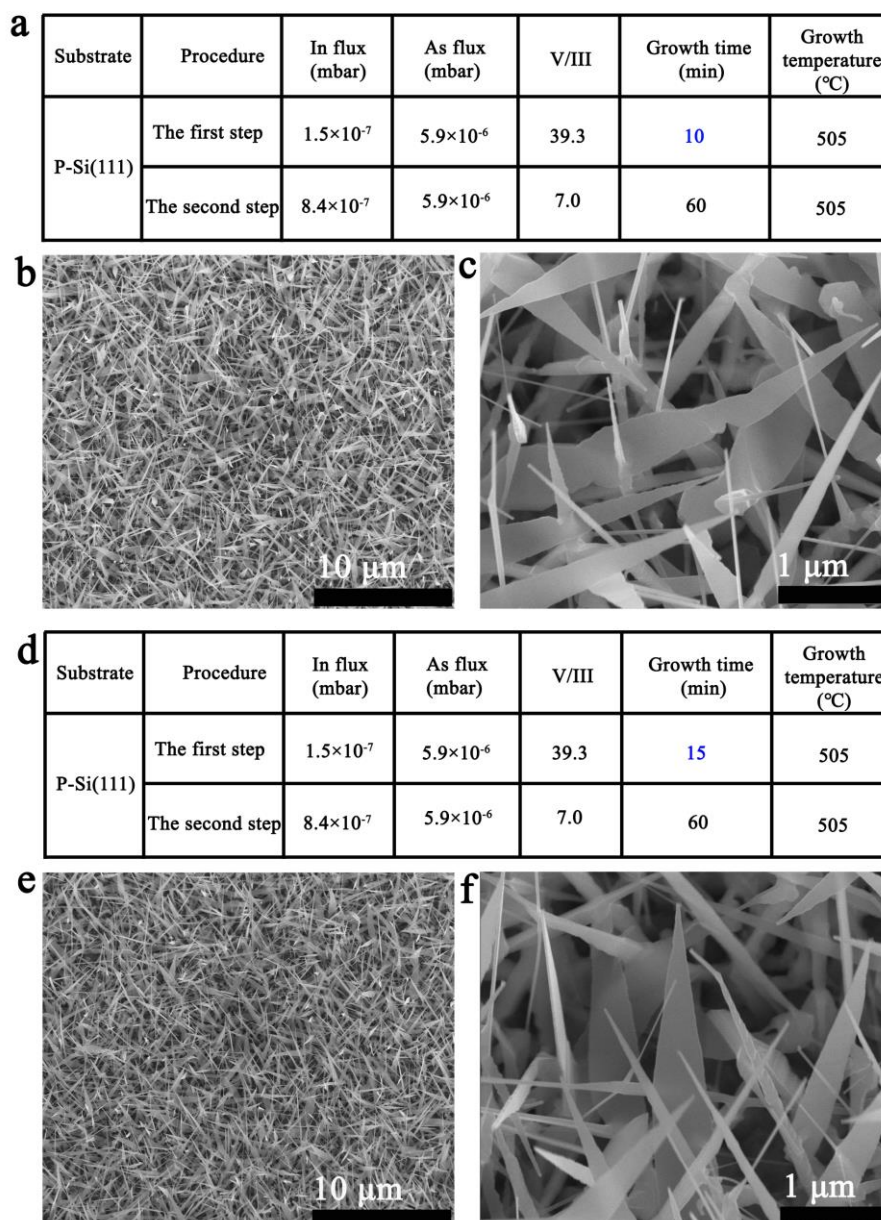
Figure S17. 2-D InAs nanosheets can be obtained by the two-step growth procedure with different InAs nanowire (the first step) growth time. **a,d**, Detailed growth conditions for the 2-D InAs nanosheet grown using the two-step growth procedure with the InAs nanowire growth time of 10 min and 15 min, respectively. **b,c** and **e,f** are corresponding 25° tilted view SEM images of the 2-D InAs nanosheets taken with different amplifications.

To exclude the possibility of the 2-D InAs nanosheets are obtained from lateral VS growth owing to the axial growth stopped by the growth condition variation, the same second-step growth has been carried out on the InAs nanowires with short growth

time. As shown in Fig. S17, it is found that the high density and large size 2-D InAs nanosheets can be obtained even the first step InAs nanowire growth time are 15 min and 10 min. If we further short the first step InAs nanowire growth time, 2-D InAs nanosheets can still be obtained, but the density of the 2-D InAs nanosheets decreases obviously. These results provide a solid evidence that the 2-D InAs nanosheets can be obtained using 'catalyst alloy segregation' with a two-step growth procedure.

S10 Wafer-scale free-standing 2-D InAs nanosheets realized by catalyst alloy segregation on various substrates

As mentioned in the main text, one of the most important characteristics for the 'catalyst segregation crystal growth' is that wafer-scale free-standing 2-D InAs nanosheets can be realized by this mechanism on various substrates with different size including Si, MgO, sapphire and GaAs *etc*. The growth parameters for the wafer-scale 2-D InAs nanosheets grown on various substrates have been summarized in Table S4. Figures S18-21 show detailed morphology information of these wafer-scale 2-D InAs nanosheets grown on the 2 inch p-type Si (111), 2 cm×2 cm MgO (100), 2 inch polished and 3 inch unpolished (growth window is 2 inch) sapphire (0001) and GaAs (100) substrates, respectively. Detailed high amplified SEM images indicate that 2-D InAs nanosheets have very homogeneous density and distribution in the different area of all these substrates.

Table S4. Summary of growth parameters for the wafer-scale 2-D InAs nanosheets grown on various substrates.

Substrates	Series	Indium flux (mbar)	Arsenic flux (mbar)	V/III	Growth time (min)	Growth temperature (°C)
Si (111)		9.3×10^{-7}	5.9×10^{-6}	6.3	40	505
MgO (100)		9.3×10^{-7}	5.9×10^{-6}	6.3	40	505
Polished Al₂O₃ (0001)	Variant substrate	9.3×10^{-7}	5.9×10^{-6}	6.3	40	505
Unpolished Al₂O₃ (0001)		9.3×10^{-7}	5.9×10^{-6}	6.3	40	505
GaAs (100)		7.4×10^{-7}	5.9×10^{-6}	8.0	40	505
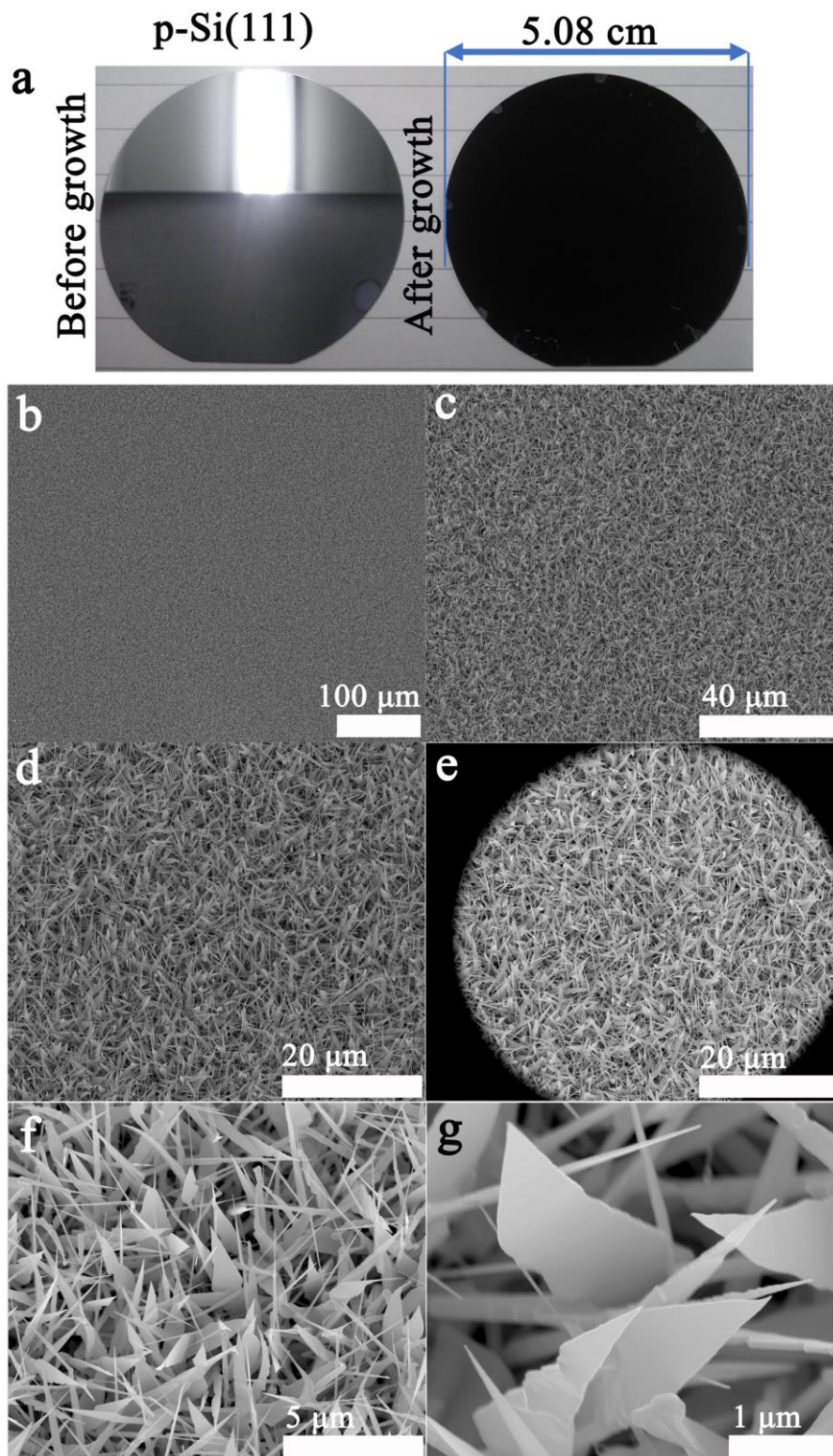
Figure S18. Wafer-scale free-standing 2-D InAs nanosheets have been realized by catalyst alloy segregation on the p-type Si (111) substrates. The InAs nanosheets were grown on the p-type Si (111) substrates with a V/III BEP ratio of 6.3 at 505 °C for 40 min. **a,** Left and right images for each panel are the substrates morphologies taken before and after sample growth with the camera of the Redmi 5 Plus, respectively. **b-g,** Typical 25° tilted view SEM images of the 2-D InAs nanosheets taken with different amplifications.
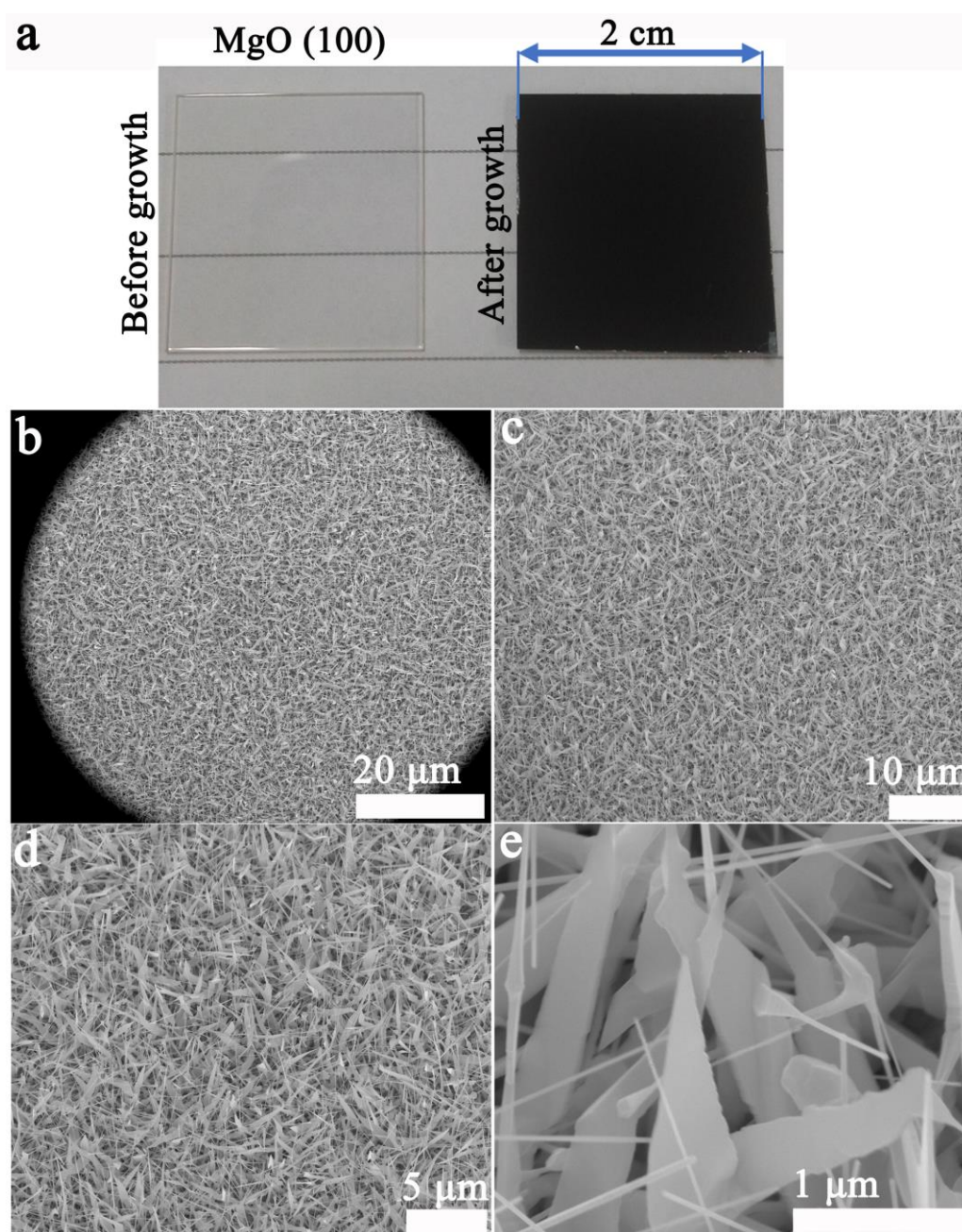
Figure S19. Wafer-scale free-standing 2-D InAs nanosheets have been realized by catalyst alloy segregation on the MgO (100) substrates. The InAs nanosheets were grown on the MgO (100) substrates with a V/III BEP ratio of 6.3 at 505 °C for 40 min. **a**, Left and right images for each panel are the substrates morphologies taken before and after growth with the camera of the Redmi 5 Plus, respectively. **b-e**, Typical 25° tilted view SEM images of the 2-D InAs nanosheets taken with different amplifications.
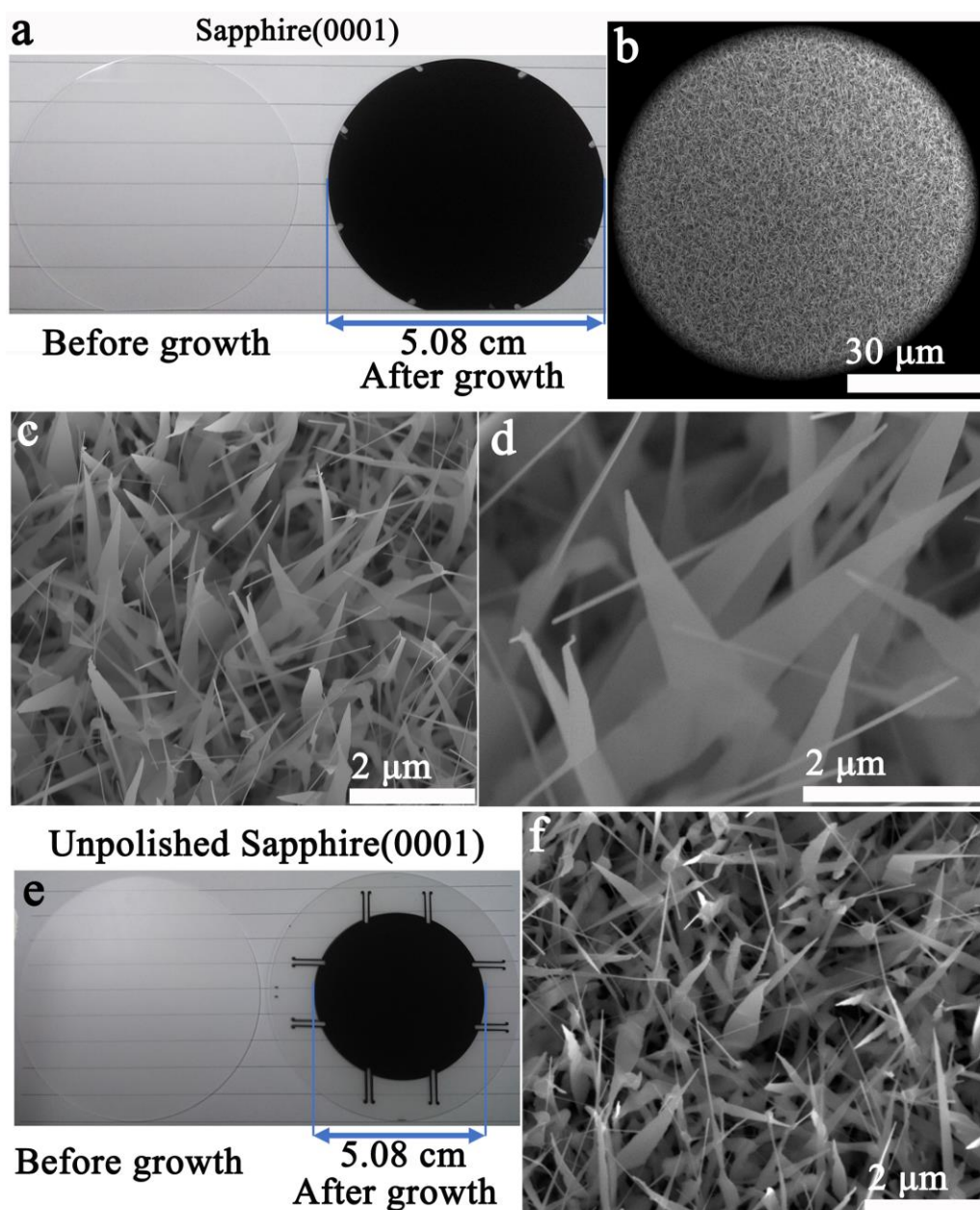
Figure S20. Wafer-scale free-standing 2-D InAs nanosheets have been realized by catalyst alloy segregation both on the polished sapphire (0001) substrates and unpolished sapphire (0001) substrates. The InAs nanosheets were grown on these sapphire substrates with a V/III BEP ratio of 6.3 at 505 °C for 40 min. **a,e**, Left and right images for each panel are the substrates morphologies taken before and after growth on the polished (a) and unpolished (e) sapphire (0001) substrates with the camera of the Redmi 5 Plus, respectively. **b-d**, Typical 25° tilted view SEM images of the 2-D InAs nanosheets grown on the polished sapphire (0001) substrates taken with different amplifications. **f**, Typical 25° tilted view SEM image of the 2-D InAs nanosheets grown on the unpolished sapphire (0001) substrates.
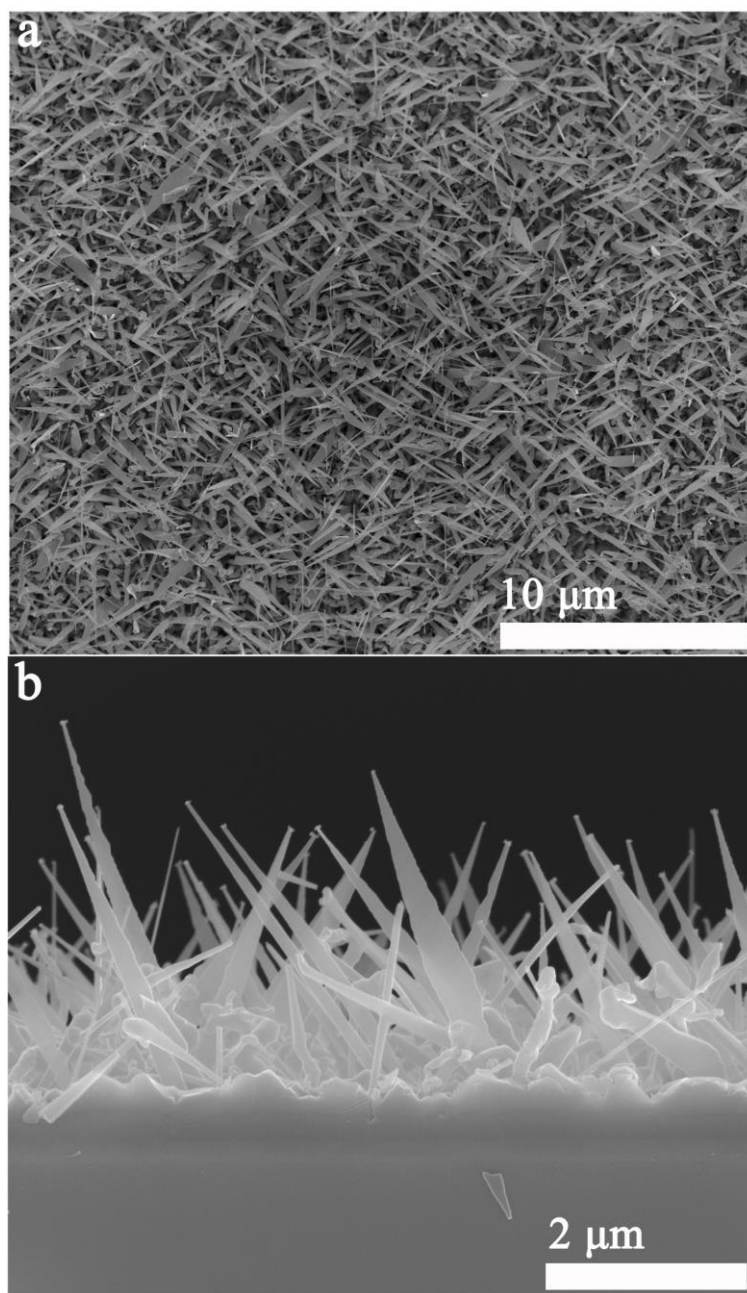
Figure S21. Wafer-scale free-standing 2-D InAs nanosheets have also been realized by catalyst alloy segregation on the GaAs (100) substrates. The InAs nanosheets were grown on the GaAs (100) substrates with a V/III BEP ratio of 8.0 at 505 °C and growth time of 40 min. **a** and **b**, 25° tilted and side view SEM images of the 2-D InAs nanosheets, respectively. The substrate morphologies taken before and after growth (not shown here) are similar to the substrate morphologies shown above.

S11 Temperature growth window for 2-D InAs nanosheets
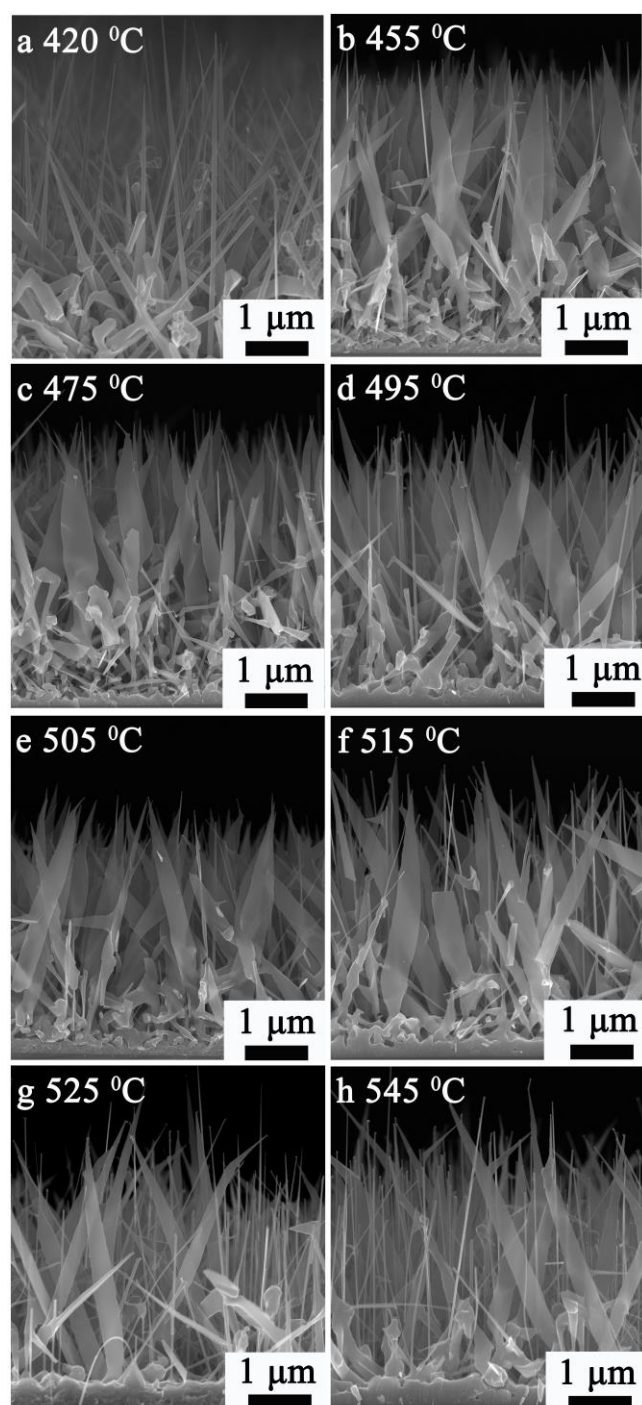
Figure S22. a-h, Side view SEM image of the InAs samples grown at indium-rich condition (indium flux: 9.3×10^{-7} mbar, arsenic flux: 5.9×10^{-6} mbar) on Si (111) substrates using silver as catalysts at different growth temperatures. The growth temperatures in (a)-(h) are 420 °C, 455 °C, 475 °C, 495 °C, 505 °C, 515 °C, 525 °C and 545 °C, respectively. For all the samples, the growth time is 40 min.

We find that the 2-D InAs nanosheets can be obtained in a large growth temperature range. Figure S22 shows the side view SEM images of the InAs samples grown at indium-rich condition (indium flux: 9.3×10^{-7} mbar, arsenic flux: 5.9×10^{-6}

mbar) on Si (111) substrates using silver as catalysts with different growth temperatures. As can be seen, InAs grown at 420 °C is 1-D nanowires and these nanowires are tapered (Fig. S22a), which indicate that no catalyst alloy segregation happens at this temperature. By increasing temperature to 455 °C (Fig. S22b), 475 °C (Fig. S22c), 495 °C (Fig. S22d), 505 °C (Fig. S22e), 515 °C (Fig. S22f), 525 °C (Fig. S22g) and 545 °C (Fig. S22h), free-standing high density 2-D InAs nanosheets can be well grown on the substrates. 1-D nanowires can be obviously observed and their density increases with increasing the growth temperature. High temperature could speed the catalyst alloy segregation process and it is the possible reason for the density increasing of the 1-D InAs nanowires.

S12 Crystal quality of the 2-D InAs nanosheets grown at low and high temperatures
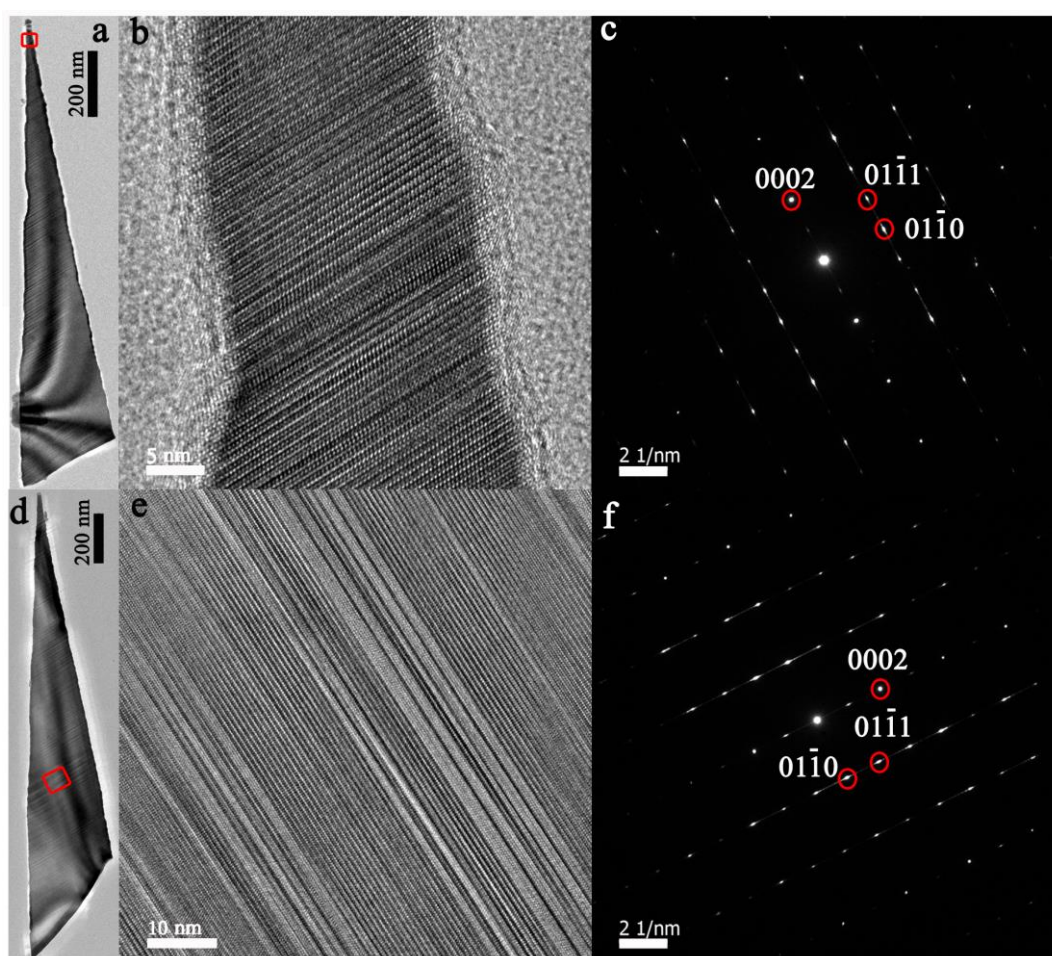
Figure S23. TEM results of 2-D InAs nanosheets grown at indium-rich condition (indium flux: 9.3×10^{-7} mbar, arsenic flux: 5.9×10^{-6} mbar) on Si (111) substrates for 40 min at 455 °C. **a** and **d** are bright-field TEM images of the InAs nanosheets and very high density of stacking faults and twin defects can be clearly observed. **b** and **e** are high-resolution TEM images taken from the nanosheets in (a) and (d), respectively. The red rectangles in (a) and (d) highlight the regions where high-resolution TEM were recorded. **c** and **f** are typical SAED patterns of the nanosheets in (a) and (d), respectively.

As mentioned in the main text, the 2-D InAs nanosheets grown at low temperatures are composed of a mixture of WZ and ZB segments. Figure S23 shows crystal-quality

and structure information of 2-D InAs nanosheets grown on Si (111) substrates at 455 °C. We can see that very high density of stacking faults and twin defects can be clearly observed in the nanosheets from high-resolution TEM images (Fig. S23b,e) and even from low magnified TEM images (Fig. S23a,d). The SAED patterns (Fig. S23c,f) recorded from the nanosheets can be indexed to the WZ phase of InAs viewed along the [2-1-10] axis. The streaks in the SAED patterns further confirm that the very high density defects appear in the nanosheets (The defect density is obvious higher than that in the samples grown at high temperatures).
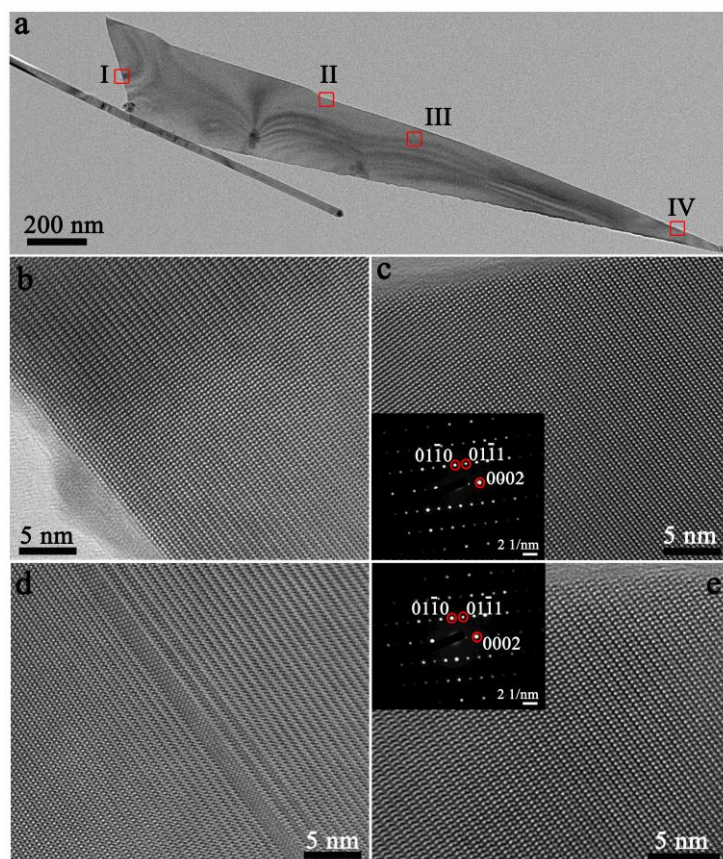
Figure S24. a, A bright-field TEM image of a 2-D InAs nanosheet grown at indium-rich condition (indium flux: 9.3×10^{-7} mbar, arsenic flux: 5.9×10^{-6} mbar) on Si (111) substrates at 545 °C for 40 min. **b-e**, High-resolution TEM images taken from bottom, center, and top of the nanosheet. The red rectangles (**I-IV**) highlight the regions where high-resolution TEM were recorded. Insets in c and e are the typical SAED patterns of the nanosheet. Only one ZB section appears in the nanosheet along its entire length.

The defect density of the nanosheets grown at different temperatures can be estimated according to their TEM images. For example, as shown in Fig. 5b in the main text, for InAs nanosheets grown at 475 °C, about 100 stacking faults and twin defects can be observed at the top section of the nanosheet within 360 nm in length. From Fig. 5f in the main text, we can see that the density of defects is obviously reduced for the nanosheet grown at 505 °C. The numbers of the stacking faults and twin defects are about 30 at the top section of the nanosheet within 310 nm in length. Further increasing the growth temperature to 525 °C, the density of stacking faults is strongly reduced (Fig. 5j in the main text). The numbers of the stacking faults and

twin defects are about 9 at the top section of the nanosheet within 1 μm in length. At high growth temperatures (e.g. 545 °C), SAED patterns and HRTEM results (Fig. 5o,p in the main text and Fig. S24) indicate that nanosheets have high crystal-quality with only one or nearly no stacking faults and other defects along their entire length. In a word, we find that increasing growth temperature can truly improve the quality of InAs nanosheets, which is consistent with the results of electrical properties and electro-optical characteristics of InAs nanosheets grown at different temperatures.

As mentioned above, Fig. S24 shows a 2-D InAs nanosheet grown at indium-rich condition (indium flux: 9.3×10^{-7} mbar, arsenic flux: 5.9×10^{-6} mbar) on Si (111) substrates at 545 °C. High-resolution TEM images have been taken from different regions of the nanosheet carefully and we find that the only one ZB section appears in the nanosheet as shown in Fig. S24d. As mentioned in the main text, pure silver nanoparticles can be segregated from catalyst alloy of the 2-D InAs nanosheets. 1-D InAs nanowire growth is seeded by these new silver nanoparticles. One of this kind of 1-D InAs nanowires can be seen from Fig. S24a. High-resolution TEM images taken from center (Fig. S25a) and top (Fig. S25b) regions of this nanowire indicate that the nanowire also has high crystal-quality.
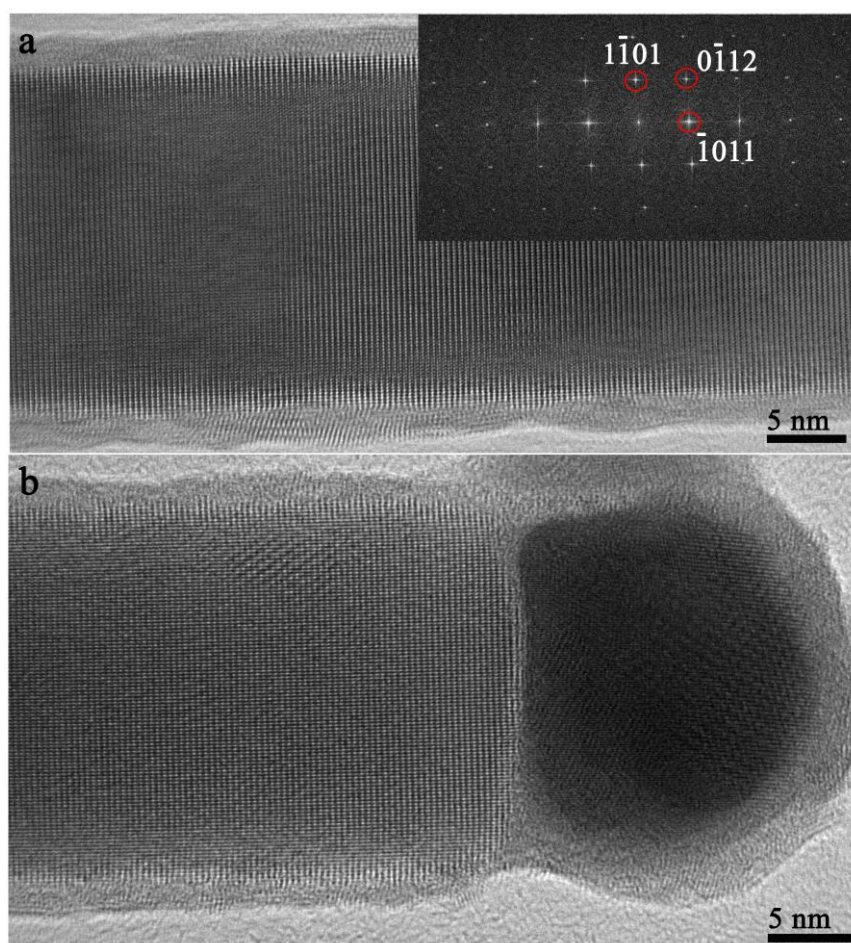
Figure S25. a,b, High-resolution TEM images taken from center and top regions of the 1-D InAs nanowire in Fig. S24a, respectively. The inset is the fast Fourier transform of (a).

Pure ZB InAs nanosheets can also be obtained for the samples grown at high

temperatures. Figure S26a is a 2-D InAs nanosheet grown at indium-rich condition (indium flux: 9.3×10^{-7} mbar, arsenic flux: 5.9×10^{-6} mbar) on Si (111) substrates with growth temperature of 545 °C. Figure S26b-j is SAED patterns taken from different areas of the InAs nanosheet as indicated by the red squares (1, 2, 3, 4, 5, 6, 7, 8 and 9, respectively). The SAED patterns recorded from these spots of the nanosheet are identical and can be indexed to the face-centered cubic phase of InAs viewed along the [011] axis. The single set of diffraction spots and detailed high-resolution TEM images taken from bottom (Fig. S26k), center (Fig. S26l), top (Fig. S26m), and side (Fig. S26n) of the nanosheet further indicate that the nanosheet is a single crystal, free of twin defects and stacking faults.
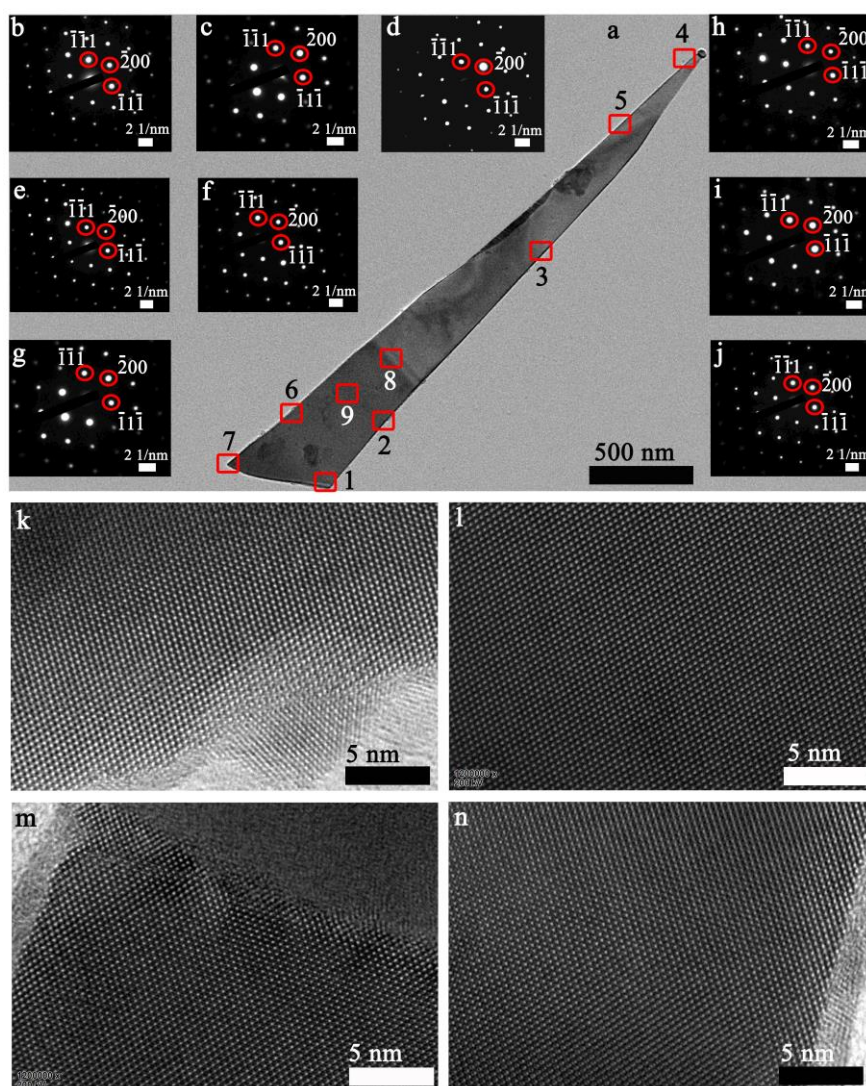
Figure S26 a, A bright-field TEM image of a 2-D InAs nanosheet grown at indium-rich condition (indium flux: 9.3×10^{-7} mbar, arsenic flux: 5.9×10^{-6} mbar) on Si (111) substrates at 545 °C for 40 min. The red rectangles highlight the regions where SAED patterns were recorded. **b-j**, SAED patterns taken along the [011] axis from regions 1, 2, 3, 4, 5, 6, 7, 8 and 9, respectively. **k-n**, High-resolution TEM images taken from bottom (k), center (l), top (m), and side (n) regions of the nanosheet.

S13 Crystal quality of the 2-D InAs nanosheets grown at a large indium flux and low temperature
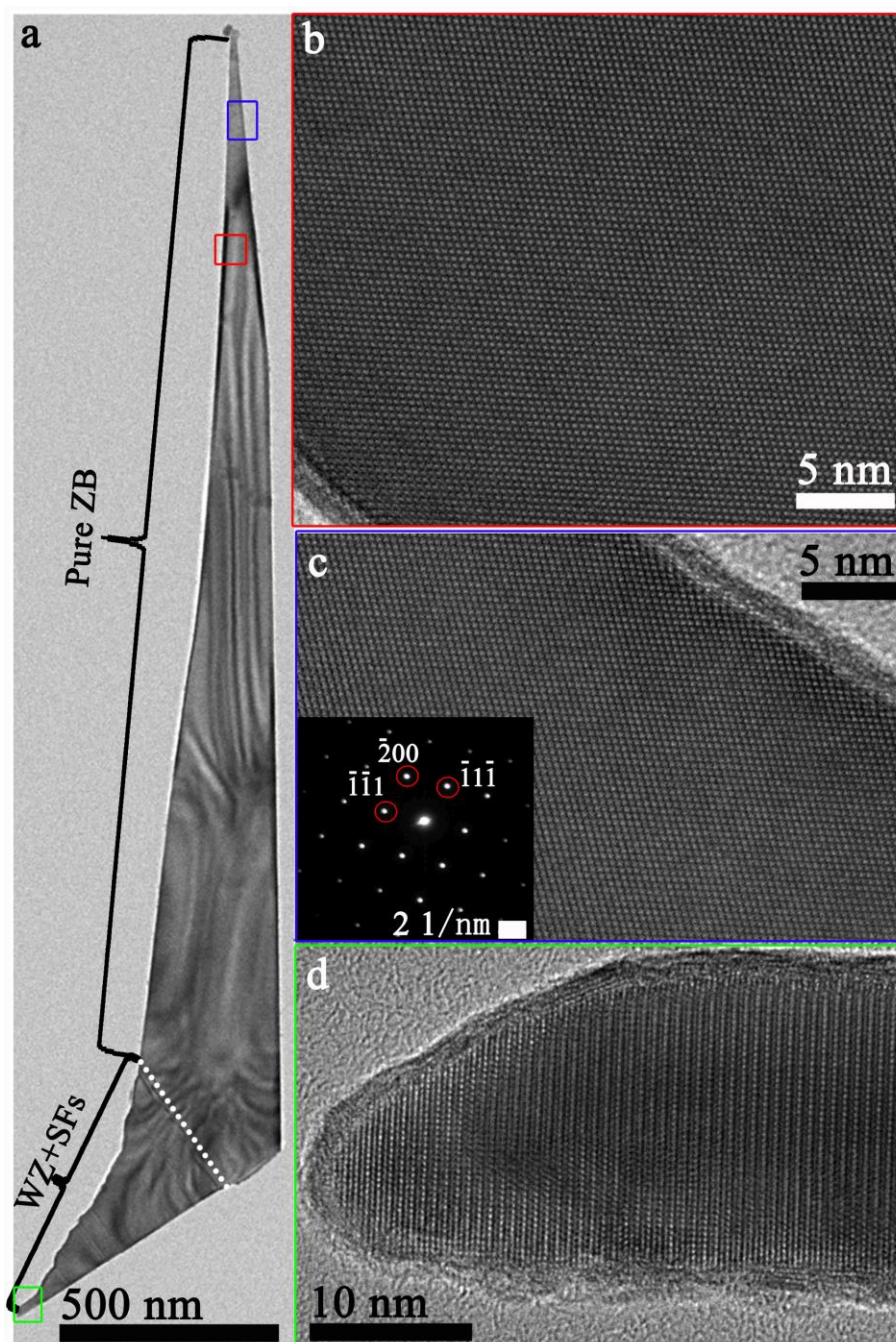
Figure S27. a, A bright-field TEM image of a 2-D InAs nanosheet grown at a large indium flux and low temperature (indium flux: 1.1×10^{-6} mbar, arsenic flux: 5.9×10^{-6} mbar; growth temperature: 505 °C) on Si (111) substrates for 40 min. The rectangles highlight the regions where high-resolution TEM images were recorded. **b-d**, High-resolution TEM images taken from left and right sides (red and blue rectangles, respectively) and bottom (green rectangle) of the nanosheet. The inset in (c) is a SAED pattern of the nanosheet taken along the [011] axis.

We find that the V/III BEP ratio (varying the indium flux and keeping the arsenic flux constant) is not very sensitive to the crystal-quality of the 2-D InAs nanosheets. As shown in Fig. 2 in the main text, the structures are all composed with WZ and ZB

mixture phases with the indium flux increasing from 4.9×10^{-7} mbar to 9.3×10^{-7} mbar. To our surprising, if we further increasing the indium flux to 1.1×10^{-6} mbar (V/III=5.4), the crystal-quality can be much improved even for the sample grown at a low temperature (505 ℃). As shown in Fig. S27, high-resolution TEM and SAED results reveal that the 2-D InAs nanosheet grown at this condition is of a pure ZB crystal structure, with the exception of a very short defect (WZ and stacking faults) section at the tail.

S14 Device fabrications and device parameters
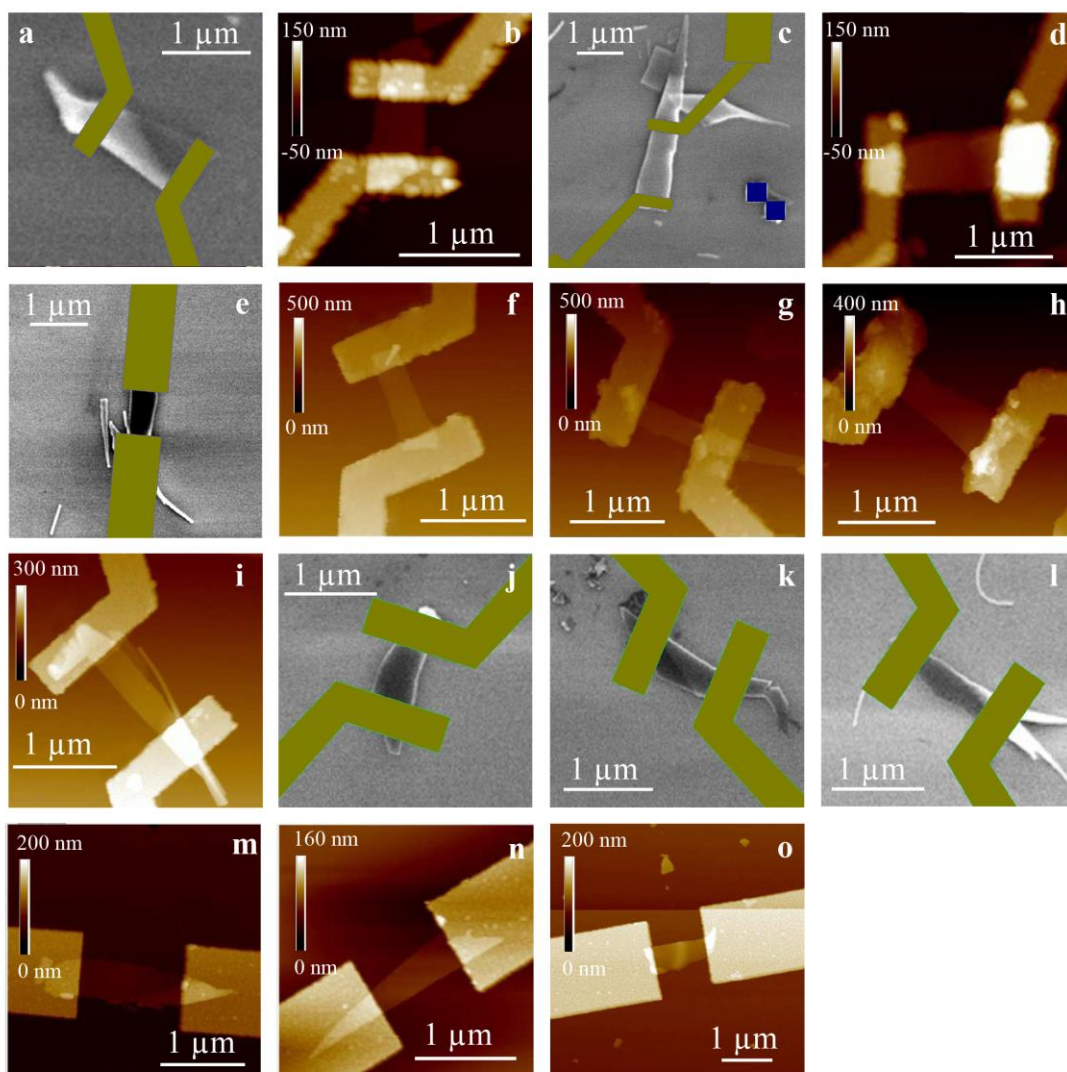
Figure S28. SEM or AFM images of the InAs nanosheet devices measured in this work: **a**, SEM image of devices A-01. **b**, AFM image of device A-02. **c**, SEM image of device A-03. **d**, AFM image of device A-04. **e**, SEM image of device A-05. **f-i**, AFM images of devices B-01, B-02, B-03 and C-01. **j-l**, SEM images of devices C-02, C-03 and C-04. **m-o**, AFM images of devices D-01, D-02 and D-03.

Figure S28 shows SEM or atomic force microscopy (AFM) images of the fabricated devices measured in this work. It is noted that some devices are broken during electrical measurements and therefore SEM images of those broken devices

are used in Fig. S28. The devices are fabricated on Si/SiO$_2$ substrates. SEM is used to locate the positions of InAs nanosheets relative to pre-defined marks. Then, electron beam lithography is used to expose the source-drain contact regions. Subsequently, we deposit 5-nm-thick titanium and 90-nm-thick gold using electron beam deposition. Before the metal deposition, the contact regions are etched in diluted (NH$_4$)$_2$S$_x$ solution to remove intrinsic oxide layers[12]. The device fabrication is finished after lift-off process. Table S5 gives measured device size parameters of channel length L (distance between the two contact electrodes), width W and thickness T. The device size parameters can be used to deduce the parameter C_g, which is the capacitance between backgate and an InAs nanosheet, by viewing the backgate-to-nanosheet structure as a parallel plate capacitor. The deduced parameter C_g will be used to extract the electron mobility in Section 15.

Table S5. Measured size parameters (channel length L, width W, thickness T) of the devices studied in this work. The parameters are obtained from the SEM or AFM images shown in Fig. S28.

Device	A-01	A-02	A-03	A-04	A-05	B-01	B-02	B-03
L (nm)	809	460	1320	995	608	708	668	1035
W (nm)	602	417	615	608	506	304	262	393
T (nm)	50~100	20	53	54	25	22	20	25

Device	C-01	C-02	C-03	C-04	D-01	D-02	D-03
L (nm)	955	553	592	760	1222	912	1025
W (nm)	295	487	419	288	430	316	473
T (nm)	25	22	19	13	12	20	21

S15 Extraction of the field-effect mobility of the InAs nanosheet devices

Here, we assume that our InAs nanosheet devices can be considered as planar field-effect transistors. Under this assumption, the source-drain current I_{sd} through an InAs nanosheet device under an applied source-drain voltage V_{sd} follows[13]

$$I_{sd} = \mu \frac{V_{sd}}{L^2} C_g (V_g - V_{th}), \tag{1}$$

Where μ is the mobility in the nanosheet, C_g is the unit area capacitance of the back

gate to the nanosheet, V_g is the voltage applied to the back gate, and V_{th} is the

threshold voltage at which the channel current is cut off. The conductance of the nanosheet device is given by

$$G_s = \frac{I_{sd}}{V_{sd}} = \frac{\mu}{L^2} C_g (V_g - V_{th}).$$ (2)

If we take contact resistance into account, the conductance of the device is

$$G = \frac{1}{G_s^{-1} + R_c}.$$ (3)

Eqs. (2) and (3) are used to fit the transfer characteristic curves to extract the mobility μ, contact resistance R_c and threshold voltage V_{th} for our fabricated InAs nanosheet devices. Taken as an example, we show in Fig. S29, how the mobility of the nanosheet in device B-01 is extracted from the measured transfer curve. Here, in Fig. S29, the blue circles are measured data of the conductance G of the device at different back gate voltage at T=40 K. The red curve shows the result of fitting to the measured data by using Eq. (3). The mobility (often referred to as the field effect mobility), together with the contact resistance and the gate threshold voltage, are extracted from the fitting. In Fig. 6e of the main article, the mobility values extracted in this way for the devices discussed in the main article at different temperatures are presented.
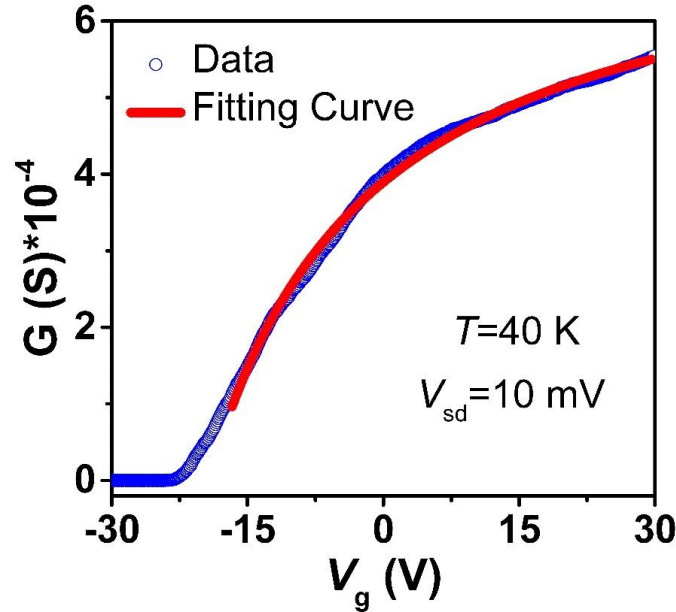
Figure S29. Measured conductance (blue circles) of device B-01 as a function of back gate voltage V_g at T=40 K. The red curve shows the results of fitting measured data to Eq. (3).
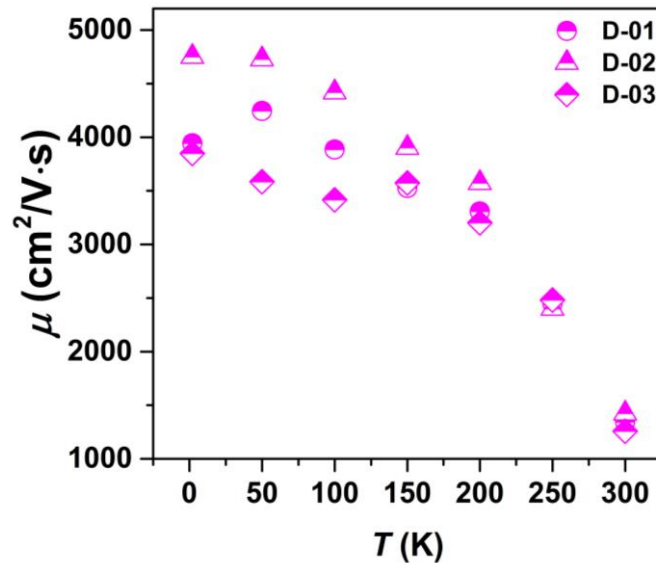
Figure S30. Extracted field-effect mobility as a function of temperature for three devices made from InAs nanosheets grown at 475 °C with a V/III BEP ratio of 6.3.

Figure S30 shows the extracted field effect mobility as a function of temperature for three devices made from InAs nanosheets grown at 475 °C with a V/III BEP ratio of 6.3. The AFM images of corresponding devices are shown in Fig. S28m-o. These devices exhibit a field-effect mobility of ~4500 cm^2/Vs at T = 2 K and ~1300 cm^2/Vs at room temperature. These values fall in between the mobility values of InAs nanosheets grown at 455 °C and 545 °C, verifying that InAs nanosheetes grown at an elevating growth temperature have an improved quality.

References:

(1) Jr., C. S. Ponseca; Němec, H.; Wallentin, J.; Anttu, N.; Beech, J. P.; Iqbal, A.; Borgström, M.; Pistol, M.-E.; Samuelson, L.; Yartsev, A. Bulk-like transverse electron mobility in an array of heavily n-doped InP nanowires probed by terahertz spectroscopy. *Phys. Rev. B* **2014**, *90*, 085405.

(2) Zhang, W.; Zeng, X.; Su, X.; Zou, X.; Mante, P.-A.; Borgström, M. T.; Yartsev, A. Carrier recombination processes in gallium indium phosphide nanowires. *Nano Lett.* **2017***, 17*, 4248.

(3) Pan, D.; Fu, M. Q.; Yu, X. Z.; Wang, X. L.; Zhu, L. J.; Nie, S. H.; Wang, S. L.; Chen, Q.; Xiong, P.; von Molnár, S.; Zhao, J. H. Controlled synthesis of phase-pure InAs nanowires on Si(111) by diminishing the diameter to 10 nm. *Nano Lett.* **2014**, *14,* 1214.

(4) Dick, K. A.; Deppert, K.; Martensson, T.; Mandl, B.; Samuelson, L.; Seifert, W. Failure of the vapor-liquid-solid mechanism in Au-assisted MOVPE growth of InAs nanowires. *Nano Lett.* **2005**, *5*, 761.

(5) Zhou, C.; Zheng, K.; Lu, Z. Y.; Zhang, Z.; Liao, Z. M.; Chen, P. P.; Lu, W.; Zou, J. Quality control of GaAs nanowire structures by limiting As flux in molecular beam epitaxy. *J. Phys. Chem. C* **2015**, *119*, 20721.

(6) Glas, F.; Harmand, J. C.; Patriarche, G. Why does wurtzite form in nanowires of III-V zinc blende semiconductors? *Phy. Rev. Lett.* **2007**, *99*, 146101.

(7) P. Lejček, *Grain Boundary Segregation in Metals* (Springer, Berlin, 2010).

(8) Baierlein, R. The elusive chemical potential. *Am. J. Phys.***2001**, *69*, 423.

(9) van de Walle, A. Multicomponent multisublattice alloys, nonconfigurational entropy and other additions to the Alloy Theoretic Automated Toolkit. *Calphad* **2009**, *33*, 266.

(10) Clyne, T. W.; Kurz, W. Solute redistribution during solidification with rapid solid state diffusion. *Metall. Trans. A* **1981**, *12*, 965.

(11) Massalski, T. B.; Okamoto, H.; Subramanian, P. R.; Kacprzak, L. Binary Alloy Phase Diagrams (ASM International, 1990).

(12) Suyatin, D. B., Thelander, C., Björk, M. T., Maximov, I. & Samuelson, L. Sulfur passivation for ohmic contact formation to InAs nanowires. *Nanotechnology* **2007**, *18*, 105307.

(13) Pan, D., Fan, D. X., Kang, N., Zhi, J. H., Yu, X. Z., Xu, H. Q., Zhao, J. H. Free-standing two-dimensional single-crystalline InSb nanosheets. *Nano Lett.* **2016**, *16*, 834.